



HAL
open science

High Resolution Crystal Structures Leverage Protein Binding Affinity Predictions

Simon Marillet, Pierre Boudinot, Frédéric Cazals

► **To cite this version:**

Simon Marillet, Pierre Boudinot, Frédéric Cazals. High Resolution Crystal Structures Leverage Protein Binding Affinity Predictions. [Research Report] RR-8733, Inria. 2015. hal-01159641v2

HAL Id: hal-01159641

<https://inria.hal.science/hal-01159641v2>

Submitted on 25 Sep 2015

HAL is a multi-disciplinary open access archive for the deposit and dissemination of scientific research documents, whether they are published or not. The documents may come from teaching and research institutions in France or abroad, or from public or private research centers.

L'archive ouverte pluridisciplinaire **HAL**, est destinée au dépôt et à la diffusion de documents scientifiques de niveau recherche, publiés ou non, émanant des établissements d'enseignement et de recherche français ou étrangers, des laboratoires publics ou privés.



High Resolution Crystal Structures Leverage Protein Binding Affinity Predictions

Simon Marillet and Pierre Boudinot and Frédéric Cazals

**RESEARCH
REPORT**

N° 8733

September 2015

Project-Team Algorithms-
Biology-Structure

ISRN INRIA/RR--8733--FR+ENG

ISSN 0249-6399



High Resolution Crystal Structures Leverage Protein Binding Affinity Predictions

Simon Marillet* and Pierre Boudinot[†] and Frédéric Cazals[‡]

Project-Team Algorithms-Biology-Structure

Research Report n° 8733 — version 2 — initial version September 2015 —
revised version Septembre 2015 — 42 pages

Abstract: Predicting protein binding affinities from structural data has remained elusive, a difficulty owing to the variety of protein binding modes. Using the structure-affinity-benchmark (SAB, 144 cases with bound/unbound crystal structures and experimental affinity measurements), prediction has been undertaken either by fitting a model using a handful of pre-defined variables, or by training a complex model from a large pool of parameters (typically hundreds). The former route unnecessarily restricts the model space, while the latter is prone to overfitting.

We design models in a third tier, using twelve variables describing enthalpic and entropic variations upon binding, and a model selection procedure identifying the best sparse model built from a subset of these variables. Using these models, we report three main results. First, we present models yielding a marked improvement of affinity predictions. For the whole dataset, we present a model predicting K_d within one and two orders of magnitude for 48% and 79% of cases, respectively. These statistics jump to 62% and 89% respectively, for the subset of the SAB consisting of high resolution structures. Second, we show that these performances owe to a new parameter encoding interface morphology and packing properties of interface atoms. Third, we argue that interface flexibility and prediction hardness do not correlate, and that for flexible cases, a performance matching that of the whole SAB can be achieved. Overall, our work suggests that the affinity prediction problem could be partly solved using databases of high resolution complexes whose affinity is known.

Key-words: Binding affinity prediction, protein flexibility, atomic packing, high resolution crystallography, linear regression

* Inria

[†] INRA, Unité de recherche Virologie et Immunologie Moléculaires

[‡] Inria

**RESEARCH CENTRE
SOPHIA ANTIPOLIS – MÉDITERRANÉE**

2004 route des Lucioles - BP 93
06902 Sophia Antipolis Cedex

L'utilisation de structures cristallographiques à haute résolution améliore la prédiction d'affinité de complexes protéine - protéine

Résumé : La prédiction d'affinité de liaison entre deux protéines à partir de données structurales reste difficile, en raison de la variété des modes d'appariement de deux protéines. À partir des données du *structure-affinity-benchmark* (SAB, 144 entrées comprenant les structures liées et non liées, ainsi que des mesures d'affinité expérimentales), la prédiction a été abordée soit en ajustant un modèle utilisant un petit nombre de variables prédéfinies, soit en entraînant un modèle complexe à partir d'un ensemble de paramètres de grande taille. Alors que la première stratégie restreint inutilement l'espace des paramètres, la seconde est encline au sur-apprentissage.

Ce travail propose des modèles dans un troisième registre, en utilisant douze variables décrivant les variations d'enthalpie et d'entropie intervenant lors de l'appariement, et une stratégie de sélection de modèle permettant d'identifier les meilleurs modèles parcimonieux construits à partir d'un sous-ensemble de ces variables. En utilisant ces modèles, nous rapportons ici trois résultats principaux. Premièrement, nous présentons des modèles permettant une nette amélioration des prédictions. Pour le jeu de données SAB complet, nous présentons un modèle capable de prédire le K_d à un et deux ordres de grandeur près pour respectivement 48% et 79% des complexes. Ces statistiques passent à respectivement 62% et 89% pour les structures à haute résolution du SAB. Deuxièmement, nous expliquons que ces performances sont dues à un nouveau paramètre codant pour la morphologie de l'interface et les propriétés de packing des atomes interfaciaux. Troisièmement, nous montrons que la flexibilité de l'interface et la difficulté à prédire l'affinité ne sont pas corrélées, et que, pour les cas flexibles, nos modèles exhibent une performance égale à celle obtenue sur le SAB complet. Plus généralement, notre travail suggère que le problème de prédiction de l'affinité pourrait être en partie résolu par l'utilisation de bases de données de complexes à haute résolution dont l'affinité serait connue.

Mots-clés : Prédiction d'affinité de liaison, flexibilité des protéines, packing atomique, cristallographie à haute résolution, régression linéaire

Contents

1	Introduction	4
1.1	Estimating Binding Affinities	4
1.2	Contributions	5
2	Estimating Affinities: Datasets and Parameters	6
2.1	Datasets from the Structure Affinity Benchmark	6
2.2	Parameters involved in Affinity Prediction Models	6
2.2.1	Key Geometric Constructions	6
2.2.2	Partners: Enthalpic Contributions	7
2.2.3	Partners: Entropic Contributions	7
2.2.4	Solvent Interactions and Electrostatics	8
2.3	Parameters Computation	8
2.4	Statistical Methodology	9
3	Results	10
3.1	Specific predictive Models yield Enhanced Correlations...	10
3.2	... and Improved Predictions on a per Complex Basis	11
3.3	Accounting for Interface Morphology and Packing Boosts Performances	12
4	Discussion and Outlook	13
5	Artwork	16
6	Supplemental	25
6.1	Datasets from the Structure Affinity Benchmark	25
6.2	Resolution of Crystal Structures in the Affinity Benchmark	26
6.3	Methods used in Previous Studies	26
6.3.1	From reference [39]	26
6.3.2	From reference [30]	27
6.3.3	From reference [51]	27
6.3.4	From reference [33]	28
6.3.5	From reference [21]	29
6.4	Statistical Methodology	29
6.4.1	Algorithms	29
6.4.2	Predictive models and their Complexity	32
6.4.3	Computing Correlation and Prediction Errors for Repeated Cross-validation	33
6.5	Results: Specific Predictive Models	33
6.6	Results: Correlation and comparison with previous work	34
6.7	Results: Correlations between individual variables and/or measured affinity	36
6.8	Results: Validation on an External Dataset	37
6.9	Results: On the Quality of Individual Predictions	38

1 Introduction

1.1 Estimating Binding Affinities

Deciphering the dynamics of protein - protein interactions is a major challenge for functional genomics, as they determine almost all processes in living organisms. If structural models of complexes shed light on interactions at the atomic level, the formation of a complex and its stability are explained by its binding affinity (affinity for short). Estimating affinities is thus a central step while modeling biological systems, to eventually unravel the hidden complexity of the interactome [4]. But such estimates are also key to exert exogenous control on biological systems in general and in medicine in particular, where the importance of designing drugs [12, 24], therapeutic peptides [44], or high affinity antibodies [34] cannot be overstated.

Affinities measured by dissociation constants (K_d) span 11 orders of magnitude, a range illustrating the diversity of biological processes and the various binding modes inherent to them. From an experimental standpoint, affinities can be measured by various techniques, including ITC, SPR, and titration by fluorescence, with free energy typical errors in the range 0.1 - 0.25 kcal/mol [24, 32, 14]. While such errors modestly impact K_d (factor of 1.52 for 0.25 kcal/mol), experimental conditions and in particular concentration, temperature, ionic strength, or pH may trigger important changes, up to 2.3kcal/mol (factor of 48 on K_d) [32].

From a modeling perspective, the estimation of affinities relies on structure based modeling, to bridge the gap between 3D atomic coordinates and thermodynamics. More precisely, consider two species A and B forming a complex C. The aforementioned dissociation constant K_d is defined by $K_d = [A][B]/[C]$, and the corresponding dissociation free energy ΔG_d , in the $c^\circ = 1M$ standard state satisfies

$$\Delta G_d = -RT \ln K_d/c^\circ = \Delta H - T\Delta S. \quad (1)$$

This equation shows that ΔG_d has two components coding the enthalpic and entropic changes upon binding, to be estimated from atomic coordinates. It also illustrates *enthalpy - entropy* compensation phenomenon [37, 18], which stipulates that a favorable enthalpic change upon association is accompanied by an entropic penalty. In fact, affinity enhancement may have an entropic origin, since a limited entropic loss may be associated with preconfigurations of specific binding sites [43, 12, 47].

In theory, estimating a dissociation free energy can be done using free energy calculations methods such as thermodynamic integration, umbrella sampling, or potential of mean forces [22, 13]. While in principle highly accurate, these methods are extremely demanding in terms of sampling, at the expense of high computational requirements to generate appropriate sampling. They are not suitable to large scale studies, which motivated the development of estimation methods focusing on relevant phenomena. For this reason, ΔG_d are generally modeled by a generic equation with terms accounting for the (variation of the) potential energy and entropy of the solute (partners and complex), as well as a solvation term [24]. Modeling enthalpic changes requires approximating the internal energy of the system. This may be done using classical force fields such as CHARMM [6], AMBER [16] or GROMOS [27], which incorporate terms accounting for van der Waals interactions, electrostatic interactions, as well as bonded interactions. One may also use phenomenological functions modeling relevant phenomena [31], including interfacial properties [1], biophysical properties such as salt bridges and hydrogen bonds or cavities [21], conservation of a.a. [26], or hot spots which may account for a large fraction of the interaction energy [40]. The solvation terms include both energetic and entropic terms, the latter referring to the loss of degrees of freedom incurred by water molecules surrounding the solute, usually estimated by weighted surface area terms [19]. Finally, the entropic variation of the

partners includes translational and rotational entropy, conformational entropy (e.g., rotameric states), and vibrational entropy. Coming up with reliable estimates for entropic change poses major challenges, yet such computations are indispensable, since as discussed above, affinity enhancement may have an entropic origin.

For large scale protein binding affinity studies, prediction models may be classified into two classes (see also the supplemental Section *Methods used in Previous Studies*). The first class consists of models using a small number of variables aiming at explaining intuitively important components of the affinity. Based on the observed correlation between the buried surface area (BSA) at the interface and binding affinity [15], a model splitting the BSA into polar and apolar components was first proposed [29]. A refinement of BSA models with a term coding the *depth* of interface atoms, called the *Voronoi shelling order*, was proposed [5], yielding improvements in particular for rigid cases. The previous models focusing on interfacial properties only, terms coding the percentage of charged and polar a.a. on the interacting surface (NIS) were introduced in [33], and their connexion with solvent dynamics investigated in [49]. Finally, a model also taking into account the iRMSD, namely the root-mean-square displacement of the C α atoms of interfacial residues between the bound and unbound states, was recently proposed [30].

The second class consists of models using machine learning techniques to select the most relevant features amidst a large pool of parameters. In [39], a binding affinity predictor based upon four machine learning classifiers is proposed. These classifiers were trained on 57 complexes (with high confidence on affinity), so as to select features amidst 200 candidates. In a nearby vein, a scoring function based model using statistical potential, for a total of 1092 parameters, was proposed in [51]. In a similar spirit, yet using a smaller set of features targeting various aspects of protein structures (H bonds, vdW interactions, cavities, iRMSD, dihedral angles, hot spots, a.a. propensities, electrostatics), various linear models were tested in [21]. Importantly, using a large number of variables helps to provide a detailed account of chemical properties of a.a. and atoms. Yet parameterizing such complex models is prone to overfitting, especially given the scarcity of data at hand, so that performances on external datasets are often limited.

Apart from the diversity of the models themselves, previous work may be distinguished using two aspects. First, different subsets of the SAB were used. Second, various statistical methodologies were used to assess the prediction performances. In particular, three types of cross validation were used, namely leave one out, four-fold, and five-fold. In doing so, the model is trained on a portion of the data, and the prediction performances are assessed by computing the correlation between the predicted affinities and the measured ones. Yet, while cross validation asymptotically yields consistent estimates [28], performances on datasets of small size should be interpreted with care [25], and checks on external datasets are called for [38]. In any case, a common finding of all these studies is that flexible cases of the SAB are the most difficult ones to deal with.

1.2 Contributions

In this work, we make a stride towards a better understanding of three core questions related to binding affinity predictions. The first one relates to the variables and models best suited to perform such predictions. We introduce sparse models relying on 12 variables aiming at capturing enthalpic and entropic changes upon binding. These models are used to estimate binding affinities on a per complex basis, from which an assessment at the dataset level is obtained by reporting the fraction of cases for which K_d is estimated within one, two and three orders of magnitude. The parameters used by these models describe surface areas, packing properties, and their variations at the atomic level, and solely exploiting a partition of atoms into polar and nonpolar. Using these variables, we identify *specific models* for subsets of the SAB considered by previous studies, whose performances match or outperform those previously published, in particular for flexible

and high resolution cases. Each specific model is also challenged on its non-specific datasets, to highlight the relevance of its variables in handling features specific from these datasets. In particular, this analysis singles out a novel parameter, coding the morphology and the packing properties of the interface, namely properties reminiscent of enthalpy and entropy.

The second question relates to a key difficulty in predicting affinities, namely flexibility. In previous work, flexible cases have been described as the most challenging ones. Using our models, we show that flexibility and prediction hardness do not correlate, and that for flexible cases, a performance almost matching that of the whole SAB can be achieved.

The third one pertains to the quality of predictions. For the whole dataset, we present a model predicting K_d within one and two orders of magnitude for 48% and 79% of cases, respectively. These statistics jump to 62% and 89% respectively, for the subset of the SAB consisting of high resolution structures, a marked improvement over previous work, also stressing the dependence of energies on atomic details.

2 Estimating Affinities: Datasets and Parameters

2.1 Datasets from the Structure Affinity Benchmark

We use the structure-affinity benchmark [32] (SAB, denoted SAB-A), providing 144 cases with crystal structures for the partners and the complex, as well as an experimentally measured dissociation free energy ΔG_d^{exp} . Following previous work, we extract seven *datasets* using a flexibility criterion, and one dataset of high resolution structures. These datasets are (supplemental Fig. 4): SAB-R_{1.0}, SAB-R_{1.1} and SAB-R_{1.5}, three datasets consisting of rather rigid cases; SAB-F₁ and SAB-F_{1.5}, two datasets consisting of rather flexible cases; SAB-I, a dataset consisting of intermediate cases; and SAB-A-HR, 37 high resolution entries (resolution ≤ 2.5) [21]. We also ruled out two cases with more than 20% atoms missing in the bound versus unbound forms, and three cases with an upper bound on the affinity rather than a proper value.

2.2 Parameters involved in Affinity Prediction Models

In the sequel, having presented key geometric constructions associated with solvent accessible models of the partners and of the complex, we define parameters meant to capture information on enthalpic and entropic contributions associated with complex formation (Fig. 1 and Table 1).

2.2.1 Key Geometric Constructions

Surface areas. The solvent accessible surface area (SASA for short) of a solvent accessible model is the sum of the surface areas exposed by the individual atoms. Upon complex formation, the *buried surface area* (BSA) is the surface area of the partners buried at the interface, namely the SASA lost by the individual atoms. This quantity has long been known as the simplest and most descriptive parameter of specific protein interfaces [1].

Voronoi interfaces and their shelling order (SO). In describing a protein - protein interface, various parameters are of interest beyond the mere list of atoms, namely its shape (e.g. elongated vs isotropic), its partition into a core and a rim, its curvature, or its number of patches. A parameter free *Voronoi interface model* encapsulating all these parameters into a single construction, the α -complex derived from the Voronoi (power) diagram of the atoms, has been proposed [10, 35]. In a nutshell, define the *restriction* of an atom as the intersection between

its ball in the solvent accessible model and its cell in the Voronoi diagram. The Voronoi interface identifies pairs of neighboring restrictions, such that each pair involves either two different partners or a partner and the interfacial solvent. The atoms found in at least one such pair are denoted \mathcal{I} and their complement \mathcal{I}^C . This Voronoi-based model was instrumental to show that the interface may involve atoms which do not lose solvent accessibility, and also to stress the role of water mediated contacts[10]. We note in passing that the exposed atoms in the set \mathcal{I}^C form the *non interacting surface* (NIS) [33].

Consider the BSA, and more specifically the atoms of one partner contributing to the BSA. The exposed surface of the atoms contributing to the BSA define a *binding patch* (patch for short) [5]. The *shelling order* (SO) of an atom from a patch is its least distance, counted in integer steps, to the nearest atom from the NIS. That is, the atoms on the border of the patch have a SO of 1 and the remaining ones have a $SO > 1$ (Fig. 1(B)). Thus, the SO generalizes core-rim models [31], since the rim corresponds to $SO = 1$, and the core to $SO > 1$.

Atomic packing properties. Early models to assess atomic packing properties resorted to the volume of Voronoi cells [23], preferably using the power diagram of the atoms instead of the Euclidean Voronoi diagram [3], since different atomic radii are accommodated. However, the Voronoi cell of an atom located on the convex hull of the protein (or complex) is unbounded. To avoid boundary effects, we focus in the sequel on the aforementioned atomic restrictions, whose volume can be computed accurately [9]. That is, denoting $\text{volume_bound}(a)$ (resp. $\text{volume_unbound}(a)$) the volume of the Voronoi restriction of an atom a in the bound form (resp. unbound form), the difference between these quantities defines the volume variation of this atom (Eq. (8)).

2.2.2 Partners: Enthalpic Contributions

Local interactions. The BSA alone does not account for the interface geometry, as the same surface area may be obtained for by morphologies as diverse as a perfectly isotropic patch, or a long and skinny patch, letting alone curvature. The obliviousness to interface morphology is intuitively detrimental, since morphology relates to the cooperativity of phenomena inherent to non-bonded interactions. To take into account such morphological features, a weighted average of atomic shelling orders, called the *internal path length* (IPL) was defined from the shelling order [5]¹. The IPL has been shown to improve the analysis of correlations between interface morphology against conserved residues and interfacial solvent dynamics [5].

In terms of binding energies, a limitation of IPL is that the SO of an atom does not account for the atomic environment of this atom—that is two atoms with identical SO may be located in a dense and loose environments respectively. This is detrimental since a dense packing is likely to favor local interactions, in particular van der Waals interactions. Since a packed interface is more likely to result in a high affinity, the shelling order is weighted by the inverse of the volume, yielding the *inverse volume-weighted internal path length* (Eq. (9)).

2.2.3 Partners: Entropic Contributions

Assessing entropic variations requires taking several components into account, in particular configurational entropy and vibrational entropy. Large conformational changes yielding structured elements correspond to entropic penalties, and can be assessed using the interface root mean

¹To be precise, $\text{IPL} = \sum_{a \in \mathcal{I}} \text{SO}(a)$. Note that replacing the SO of each atom by one results in the number of interface atoms, which is known to correlate with BSA for rigid cases [32].

square deviation (iRMSD). In the sequel, we refine this measure using atomic packing properties.

Packing properties. A closely packed environment yields favorable interactions by increasing the number of neighbors. But it also entails an entropic penalty for that atom, illustrating the classical enthalpy - entropy compensation, which holds in particular for biological systems involving weak interactions [18, 14]. We therefore use our atomic volumes and their variations upon binding (Eq. (8)) to model both the interaction energy and the entropic changes upon binding.

To model entropic changes, we resort to volume variations. We do so by considering four categories of atoms. For interface atoms, we define two groups, those found on the rim ($\mathcal{I}, SO = 1$), retaining solvent accessibility, and the remaining ones ($\mathcal{I}, SO > 1$). Likewise, for the set of non interface atoms, we distinguish between those retaining solvent accessibility (\mathcal{I}^C and $SASA > 0$ in the complex), and those which do not (\mathcal{I}^C and $SASA = 0$ in the complex). Adding up volume variations for these four categories of atoms yields the following four *Sum of Volumes Differences* (*SVD*) parameters, namely SVD_SO1 ($\mathcal{I}, SO(a) = 1$; Eq. (10)), SVD_SOGT1 ($\mathcal{I}, SO(a) > 1$; Eq. (11)), SVD_NI_B ($\mathcal{I}^C, SASA(a) = 0$; Eq. (12)), SVD_NI_E ($\mathcal{I}^C, SASA(a) > 0$; Eq. (13)).

2.2.4 Solvent Interactions and Electrostatics

The interaction between a protein molecule and water molecules is complex. In particular, the exposition to the solvent of non polar groups hinders the ability of water molecules to engage into hydrogen bonding, yielding an entropic loss for such water molecules. To account for these effects, we use the fractions of charged and polar a.a. on the non interacting surface [33], respectively denoted NIS^{polar} (Eq. (14)) and $NIS^{charged}$ (Eq. (15)). We also use the variation of these quantities to account for conformational changes upon binding, yielding the quantities ΔNIS^{polar} (Eq. (16)) and $\Delta NIS^{charged}$ (Eq. (17)).

To challenge a.a. terms with their atomic counterparts and see which ones are best suited to perform affinity predictions, we also included the atomic solvation energy from Eisenberg et al [20], describing the free energies of transfer from 1-octanol to water per surface unit (\AA^2). The corresponding variable, $ATOM_SOLV$, is a weighted sum of atomic solvent accessible surface areas (Eq. (18)), and may be seen as the atomic-scale counterparts of $NIS^{charged}$ and NIS^{polar} .

Finally, we include an intermediate-grained description of the non-interacting surface which consists in the atomic-wise polar area of the complex. The corresponding term, $POLAR_SASA$ (Eq. (19)), is also a weighed sum of exposed areas.

2.3 Parameters Computation

To compute the atoms at interface along with their shelling order, packing and volume, we use the application `sbl-vorshell-bp-ABW-atomic.exe` from the Structural Biology Library (SBL) [7], see <http://sbl.inria.fr>. Contacts mediated by water molecules are included because crystallographic water molecules are biologically relevant [45].

To compute the solvent accessible atoms of the molecules, we use the application `sbl-vorlume-pdb.exe` software [9], also from the SBL [7]. In that case, water molecules are not considered since they contribute to the protein surface solvation as much the bulk solvent.

2.4 Statistical Methodology

In the sequel, we explain how to predict $\Delta G_d^{exp_i}$ of complexes from a dataset \mathcal{D} . Estimation is performed on a per complex basis, from which performances at the whole dataset level will be derived. Our predictions rely on three related concepts defined precisely hereafter (see also Fig. 2):

- **Template:** a fixed set of variables from \mathcal{V} ,
- **Model:** a linear model consisting in a template plus the associated coefficients. As we shall see, such models are associated with cross-validation folds.
- **Predictive model for \mathcal{D} :** the machinery returning one binding affinity estimate \hat{g}_i per complex from \mathcal{D} , using N_{XV} repetitions of the k -fold cross validation.

Templates. Denote \mathcal{V} the pool of twelve variables specified by Eq. (9) to (19) (Table 1), plus the iRMSD defined in the SAB. Let a *template* be a set of variables, i.e. a subset of \mathcal{V} . To define parsimonious templates from the set \mathcal{V} , we generate subsets of \mathcal{V} involving up to at most five variables—an upper bound dictated by the fact that beyond five variable, the performance of the corresponding best predictive model starts to decrease (supplemental Fig. 6). This defines a pool of templates $\mathcal{T} = \{T_1, \dots, T_{1585}\}$ ².

Cross-validation. In the following a *model* is associated to both a template $T_l \in \mathcal{T}$ and a dataset \mathcal{D} from the SAB. More precisely, a model refers to a linear model, i.e. the variables of the template plus the associated coefficients.

Practically, models are defined during k -fold cross-validation (with $k = 5$), and a number of N_{XV} (=10000) of repetitions (Fig. 2). Consider one repetition, which thus consists of splitting at random \mathcal{D} into 5 subsets called folds. For one fold, a linear model associated with T_l is trained on 4/5 of the dataset \mathcal{D} , and predictions are run on the remaining 1/5 of complexes. Processing the five folds yields one repetition of the cross validation procedure, resulting in one prediction \hat{g}_{ij} for the $\Delta G_d^{exp_i}$ of each complex. The set of all predictions in one repeat, say the j th one, is denoted

$$\hat{G}_j = \{\hat{g}_{ij}\}_{i=1, \dots, |\mathcal{D}|}. \quad (2)$$

Note again that these predictions stem from k linear models associated with T_l , namely one per fold.

Statistics per template. Considering one cross-validation repetition, we define the correlation $Corr_j$ as the correlation between the experimental values $\{\Delta G_d^{exp_i}\}$ and the predictions \hat{G}_j . An overall assessment of the template T_l using the N_{XV} repetitions is obtained by the following *median of correlations* (see also the supplemental Section 6.4.3):

$$C[T_l, \mathcal{D}] = \text{median}_j \text{Corr}_j. \quad (3)$$

For a complex, we define the binding affinity *prediction* \hat{g}_i as the median across repetitions *i.e.*

$$\hat{g}_i = \text{median}_j \hat{g}_{ij}. \quad (4)$$

Likewise, the *median prediction error* is defined by

$$e_i \equiv e_i[T_l, \mathcal{D}] = \text{median}_j (\Delta G_d^{exp_i} - \hat{g}_{ij}), \quad (5)$$

²Since we have 12 variables, one has $\sum_{k=1}^5 \binom{12}{k} = 1585$.

and the *median absolute prediction error* by:

$$e_i^{\text{abs}} \equiv e_i^{\text{abs}}[T_l, \mathcal{D}] = \text{median}_j(|\Delta G_d^{\text{exp}i} - \hat{g}_{ij}|). \quad (6)$$

Using this latter value, we define the *prediction ratio* p_δ^{error} as the percentage of cases such that the dissociation free energy is off by a specified amount δ :

$$p_\delta^{\text{error}} = \% \text{cases in } \mathcal{D} \text{ such that } e_i^{\text{abs}}[T_l, \mathcal{D}] \leq \delta. \quad (7)$$

In particular, setting δ to 1.4, 2.8 and 4.2 kcal/mol in the previous equation yields cases whose K_d is approximated within one, two and three orders of magnitude respectively.

Finally, a permutation test yields a p-value for each predictive model [41]. In a nutshell, the rationale consists of generating randomized datasets by shuffling their $\Delta G_d^{\text{exp}i}$ values. Then, one computes a performance criterion for each such dataset, from which the p-value is inferred (supplement, Algorithm 1).

Model selection. Define the best predictive model as the one maximizing the median correlation $C[T_l, \mathcal{D}]$ (Eq. (3)), called the *performance criterion* for short in the sequel.

We wish to single out the best predictive models, i.e. those that cannot be statistically distinguished from the best predictive model, as just defined.

To single out such models, observe that to compare two predictive models M_{T_1} and M_{T_2} , a univariate two-sample test suffices to check whether the two sets of performances (one per model) obtained for the N_{XV} repetitions come from the same distribution (the null hypothesis H_0), or whether one dominates the other. In an analogous spirit and since we are handling a pool of predictive models \mathcal{T} , we wish to identify within \mathcal{T} a subset of predictive models whose distribution cannot be distinguished from the best predictive model. To this end, we decompose the predictive models as $\mathcal{T} = \mathcal{T}_1 \cup \mathcal{T}_2$ such that (i) the best predictive model is in \mathcal{T}_1 , (ii) in comparing two predictive models from \mathcal{T}_1 , one does not reject H_0 , and (iii) in comparing one predictive model from \mathcal{T}_1 against one predictive model from \mathcal{T}_2 , one rejects H_0 . The predictive models in \mathcal{T}_1 are called the *specific models* for the dataset \mathcal{D} . The corresponding procedure is based on the Kruskal-Wallis test (supplemental, Algorithm 2). The p-value threshold is set to $\alpha = 0.01$.

We also use the eight datasets to define the *best overall predictive model*. To this end, we sorted the models using the aforementioned performance criterion and took the model with lowest median rank among all datasets. This yields the predictive model 9 in the sequel.

3 Results

3.1 Specific predictive Models yield Enhanced Correlations...

Recall that a *dataset* can be the SAB or a subset of the SAB defined by bounds on the iRMSD or the resolution of complexes and partners. In the sequel, we analyze the performances of predictive models, as defined in the previous section.

Interestingly, a single predictive model is significantly better than the others for all datasets. These predictive models are all statistically significant with a p-value smaller than 0.01, except for the one associated with the dataset SAB-I, therefore omitted from subsequent analysis.

In terms of correlations between estimates and $\Delta G_d^{\text{exp}i}$ (supplemental Table 4, 5-fold cross validation), our specific predictive models outperform previous works in 5/8 cases. For two of the three remaining cases, the top correlation is provided by the complex model from [39],

which we estimated to use 94 variables (see supplemental Section 6.3.1). For the remaining one, [21] provides the best results with a seven variables model. Unfortunately, the corresponding variables are not specified.

In terms of correlation values themselves, three facts emerge. First, the predictive model specific of the high resolution model dataset yields a remarkable correlation of 0.77. Second, for flexible datasets, satisfactory performances are observed, which is unexpected since such cases are generally considered as the most challenging ones for affinity predictions. In particular, for flexible cases characterized by an interface iRMSD larger than 1.5Å, a correlation of 0.46 is obtained, a value comparable to that of the whole dataset, namely 0.48. Finally, the best overall predictive model, when challenged by individual datasets, shows performances comparable to those of their specific predictive models with maximum drop in correlation of 0.06. This is a clear assessment of its robustness.

3.2 ... and Improved Predictions on a per Complex Basis

The correlation between predictions and $\Delta G_d^{exp_i}$ provides a global performance assessment of a predictive model for a dataset. To gain insights at the individual complex level, we use the individual predictions \hat{g}_{ij} . Using these individual predictions, we compute the prediction ratio (Eq. 7) for $\delta = 1.4, 2.8$ and 4.2 kcal/mol, respectively, yielding the fraction of cases for which K_d is predicted within one, two and three orders of magnitude. Three striking facts emerge from Table 3.

First, the merits of our specific predictive models as well as those of the best overall predictive model clearly emerge. As a quantitative measure, we collect the min and max prediction ratios for the aforementioned three values of δ , yielding a three pairs min-max percentages. For our best overall predictive model, one gets 44-57%, 74-86% and 91-95% within one, two and three orders of magnitude. In contrast, the intervals for [33] are 46-51%, 68-83% and 85-95%, and those for [30] are 22-44%, 57-73% and 85-93%. Collecting now the min and max prediction ratios of the specific predictive models on their specific datasets, one gets 46-62%, 78-89%, 85-97%. Thus, for the whole SAB, both the specific predictive model and the best overall predictive model yield improved performances.

Second, the prediction ratios of the predictive model specific of the high resolution dataset turn out to be 62%, 89% and 97% within one, two and three orders of magnitude, an outstanding performance.

Third, concerning the flexible datasets, considered as the most challenging ones in previous studies, predictive model 7 (dataset SAB-F₁) and predictive model 8 (dataset SAB-F_{1.5}) reach performances comparable to those obtained on the whole SAB, namely $p_{1.4}^{error}$ values of 50% and 50% respectively, instead of 47%. This shows that the difficulty of predicting binding affinity for flexible interfaces can be circumvented by the right choice of variables. This observation is also backed up by the lack of correlation between the interface flexibility and the prediction error (Fig. 3). We also note in passing that this conclusion is based on the analysis of the prediction ratios of Eq. (7), rather than that of the correlation coefficients of Eq. (3) (supplemental Table 4). Correlation coefficients are indeed global indicators of the dependency between two random variables, and do not assess the predictive performances on a per-complex basis.

Specific cases. Inspecting extreme cases is informative (named cases, Fig. 3). The individual predictions \hat{g}_i from Eq. 4 are provided in the supplemental Table 9.

On the one hand, the affinity of three complexes with subpicomolar affinity (1EMV, 1BRS, 1DFJ) is significantly under-estimated (Fig. 3). These three complexes involve an inhibitor taking the place of a cognate nucleic acid. Such complexes typically involve strong electrostatic

interactions [42, 30], which are overlooked by our models. It could also be the case that such complexes manage to limit the entropic loss upon binding, possibly by transferring the dynamics of interfacial atoms to the protein’s non interacting atoms.

On the other hand, predictions are excellent for several flexible cases, in particular 1F6M and 2I9B (Fig. 3). Complex 1F6M consists of a thioredoxin reductase in flavin-reducing conformation with its substrate. The reductase switches between bound and unbound conformations using a hinge-like motion. Complex 2I9B consists of a urokinase plasminogen activator receptor and its associated ligand. There is a global conformational change of the receptor upon binding (RMSD 2.657 Å) but no obvious hinge motion. It is the only complex with an iRMSD greater than 3 Å and a prediction error below 1.4 kcal/mol.

Classically for complexes with large interfaces, affinity predictions based on the BSA often result in overestimates. Beyond a certain interface size, the affinity no longer increases as much with the interface size, a behavior which could be related to a non-uniform atomic packing at the interface [30]. However, the packing distribution of large interfaces matches that of the remaining ones (supplemental Fig. 7), and no correlation is observed between the quality of individual predictions and interface size (supplemental Fig. 8). Thus, packing heterogeneity may not account for mild to poor prediction performances in that context.

Validation on external datasets. Cross validation results obtained on datasets of small size should be interpreted with care [25], and checks on external datasets are a must [38]. We therefore ran predictions on an external dataset (supplemental Table 7), from which two striking facts emerge.

The correlations observed compare to those obtained with cross-validation, with a maximum drop of 0.11 excluding predictive models 2 and 8. For the latter two predictive models, the drop reaches 0.33 and 0.25 respectively, a fact likely related to the small size of their training datasets. Second, the proportions $p_{1.4}^{\text{error}}$, $p_{2.8}^{\text{error}}$ and $p_{4.2}^{\text{error}}$ are smaller than their cross-validated counterparts, by a factor 1.4 ($p_{4.2}^{\text{error}}$, predictive model 8) to 9.5 ($p_{1.4}^{\text{error}}$, predictive model 7). Therefore, on this external dataset, despite being good predictors on a global level, as assessed by the correlation coefficient, our predictive models do not always perform robustly on a per complex basis.

3.3 Accounting for Interface Morphology and Packing Boosts Performances

The performances of our predictive models owe to the new variables introduced in this study (Table 2). The variable selected most often is IVW-IPL (6/8 cases), stressing the role of the interface size (in terms of buried surface area), but also of atomic packing properties. The second variable selected most often is $\text{NIS}^{\text{charged}}$ (5/8 cases), highlighting the role of solvent interactions [30]. Two other variables selected for 3/8 datasets, respectively represent volume variation at the interface rim (SVD_SO1), and solvation properties of the complex at the atomic scale (ATOM_SOLV). Interestingly, inspecting these four variables reveals a correlation between IVW-IPL and SVD_SOGT1 (supplemental Table 6), so that these variables might be used interchangeably. The same observation holds for $\text{NIS}^{\text{charged}}$ and $\text{NIS}^{\text{polar}}$.

Of particular interest in this context is our best overall predictive model. This predictive model uses variables IVW-IPL, SVD_SO1 and $\text{NIS}^{\text{charged}}$ and is therefore equivalent to predictive model 4. Not surprisingly, these variables form the top three of variables selected most often by the specific predictive models (Table 2). Its performances, are similar to those of specific

predictive models on their own datasets (Table 3). Interestingly, it is a better predictor of flexible complexes than predictive model 1. Finally, its results on external datasets (Tables 7 and 8) show that it is outperformed by specific predictive models for four datasets, and outperforms them for two (not considering predictive model 6).

4 Discussion and Outlook

This work develops sparse binding affinity predictions models, which shed new light on the hardness of affinity prediction, and improve prediction quality using variables coding enthalpic and entropic variations upon binding.

On the hardness of affinity predictions. Flexible datasets have been reported as the most challenging ones in previous studies. However, as shown here, the segregation of flexible versus rigid appears partially founded, with some easy to predict flexible complexes, and some hard to predict rigid cases. This observation is not completely surprising, since conformational changes alone tell little, in particular, on entropic changes upon binding. It also hints at the possibility of improving the quality of predictions for cases with small conformational changes upon binding, as molecular dynamics simulations in the intermediate time range may provide good estimates for the entropic penalties in those cases.

On the quality of predictions. A key achievement of this study is the quality of predictions, assessed in terms of absolute error or equivalently accuracy on K_d . To summarize, two values may be put forward, namely the fraction of cases for which K_d is predicted within one and two orders of magnitude. For the best overall predictive model, these fractions, corresponding to the whole SAB, are 48% and 79%, respectively. For the predictive model specific of high resolution complexes, these fractions are 62% and 89%. These numbers clearly advance the state-of-the-art, and call for two comments.

First, our models do not take into account the pH, whose change by two units may alter K_d by a factor ten or more. Given this specificity, they second the goal set in [30], namely that of approximating K_d within two orders of magnitude.

Second, the high performance obtained for high resolution structures recalls the short range nature of selected forces—van der Waals interactions in particular, and stresses the dependence of energies on atomic details. From a quantitative standpoint, from Cruickshank’s formula, the typical precision on atomic coordinates at a resolution of say 2.5\AA lies in the range $[0.2, 0.4]\text{\AA}$ [17, 2]. At such a resolution, which is the worst used in the high resolution dataset (supplemental Fig. 5), the inter-atomic distance between non covalently bonded atoms located nearby in 3D space [10] may already be spoiled by a factor circa $\sim 1/4$ (say $2 \times 0.3/2.5$). The situation deteriorates with the resolution, with a potential significant impact on the atomic scale parameters listed in Table 1. Therefore, the incidence of resolution on prediction performance should not come as a surprise. In a more general perspective, this observation is reminiscent of the role of molecular shape in determining motions [36], and also on the importance of packing properties in protein structure [11].

One generic predictive model versus several specific predictive models. The diversity of the specific predictive models may be seen as a weakness or a strength. For the former viewpoint, one may argue that thermodynamics call for a unified model. For the latter one, given the intrinsic complexity of the problem (recall that the binding affinity is inherently coupled to a thermodynamic equilibrium), and the paucity of the dataset, it is clearly beneficial to exploit

specific features of datasets. Moreover, specific predictive models are of practical interest since to predict the affinity of a complex performing a specific biological function, one may use a dataset of complexes related to that function. Further arguments to choose between these two interpretations will likely emerge upon populating the structure affinity benchmark.

On key parameters. Our predictive models preferably use parameter IVW-IPL, and then $NIS^{charged}$. The former, introduced in this work, combines the overall shape of the interface and involves atomic packing properties. It is reminiscent of cooperativity phenomena observed for weak interactions [5]. The latter, $NIS^{charged}$, encodes the electrostatic properties of the non interacting surface, as recently investigated [49]. The following top scorers represent volume variation at the interface rim (SVD_SO1), and solvation properties of the complex at the atomic scale (ATOM_SOLV). Among these four variables, two describe surface properties at different scales (atomic for ATOM_SOLV, and at residue level for $NIS^{charged}$), and two encode interface properties, one static for the whole interface (IVW-IPL), and one dynamic for the outer layer of the interface (SVD_SO1).

Remarkably, these parameters are simple ones, derived from the Voronoi diagram of the solvent accessible models of the three structures involved (two for the partners, one for the complex). From a computational standpoint, processing a structure of say up to 10,000 atoms takes a handful of seconds on a desktop computer [9].

Outlook. Estimating binding affinities is a central endeavor to understand protein - protein interactions. Strikingly, the predictive models and variables presented here yield a prediction accuracy of 2.8 kcal/mol per complex in 79% of cases for the whole SAB, and in 89% of cases for high resolution complexes. This represent a significant progress over previous methods. Since our methods inherently exploit static properties of crystal structures, improving results even further calls for developments in two directions. On the one hand, unveiling dynamical properties of the partners and the associated complex, by sampling and modeling the associated (potential, free) energy landscapes will undoubtedly yield enhanced predictions [50]. Along the way, a central problem to be addressed is that of the potential energy model best suited, since, as shown in this work, coarse grain descriptors can match or surpass the performances of detailed chemical ones. In this respect, our ability to accurately sample [50, 13] and compare [8] sampled energy landscapes should prove critical. On the other hand, a weakness shared by our method and previous ones is the absence of terms taking into account the pH and the ionic strength – a limitation actually accounting for the poor performances observed on complexes involving significant electrostatic interactions. For such cases, incorporating terms accounting for counter-ion condensation seems critical, yet, controlling the enthalpy - entropy balance within such models remain challenging [42, 46].

The affinity prediction problem is also of special interest from the machine learning perspective. Affinity prediction is indeed modeled here a particular instance of a problem known as regression [28]. In this setting, the data is assumed to be generated by a process and applied some random noise. The most important attribute of regressors is their *consistency*, *i.e.* their ability to converge toward the true model given data accounting for the whole space. However, for a regressor to achieve consistency, the data must satisfy some assumptions. For instance it should be well distributed over the space of possible data points. In our case, this means that the dataset should evenly represent all possible protein-protein complexes. This is most probably not the case for the SAB. The availability of larger datasets will also ease the model selection problem, undertaken by complete enumeration over the parameter set in this work. In principle, sparse least square models can be obtained using regularization techniques [48]. However, the inherent randomization used by cross-validation makes model selection unstable for small datasets,

making such methods hard to use at this stage. For these reasons, sparse specific models using with relevant variables, as developed in this work, appear as a privileged solution to estimate binding affinities.

5 Artwork

Table 1 Parameters used to estimate binding affinities. Atomic level parameters: IVW-IPL, SVD_SO1, SVD_SOGT1, SVD_NI_B, SVD_NI_E, ATOM_SOLV, POLAR_SASA; Residue level parameters: NIS^{polar} , $NIS^{charged}$, ΔNIS^{polar} , $\Delta NIS^{charged}$; Interface level parameter: iRMSD. The acronyms read as follows (see text for details): **S**um of **V**olume **D**ifferences; **S**helling **O**rders; **I**nverse **V**olume **W**eighted; **I**nternal **P**ath **L**ength; **N**on **I**nteracting **B**uried/**E**xposed; **N**on **I**nteracting **S**urface; **S**olvent **A**ccessible **S**urface **A**rea;

$\Delta\text{-vol}(a) = \text{volume_bound}(a) - \text{volume_unbound}(a). \quad (8)$	$\text{IVW-IPL} = \sum_{a \in \mathcal{I}} \frac{\text{SO}(a)}{\text{volume_bound}(a)} \quad (9)$
$\text{SVD_SO1} = \sum_{a \in \mathcal{I}, \text{SO}(a)=1} \Delta\text{-vol}(a) \quad (10)$	$\text{SVD_SOGT1} = \sum_{a \in \mathcal{I}, \text{SO}(a)>1} \Delta\text{-vol}(a) \quad (11)$
$\text{SVD_NI_B} = \sum_{a \in \mathcal{I}^C, \text{SASA}(a)=0} \Delta\text{-vol}(a) \quad (12)$	$\text{SVD_NI_E} = \sum_{a \in \mathcal{I}^C, \text{SASA}(a)>0} \Delta\text{-vol}(a) \quad (13)$
$NIS^{polar} = \frac{\#\text{solvent accessible polar residues}}{\#\text{solvent accessible residues}} \quad (14)$	$NIS^{charged} = \frac{\#\text{solvent accessible charged residues}}{\#\text{solvent accessible residues}} \quad (15)$
$\Delta NIS^{polar} = NIS_{bound}^{polar} - NIS_{unbound}^{polar} \quad (16)$	$\Delta NIS^{charged} = NIS_{bound}^{charged} - NIS_{unbound}^{charged} \quad (17)$
$\text{ATOM_SOLV} = \sum_{a \in \mathcal{I}^C} \text{SASA}(a) \cdot \sigma(a) \quad (18)$	$\text{POLAR_SASA} = \sum_{a \in \mathcal{I}^C \text{ and } \sigma(a)<0} \text{SASA}(a) \quad (19)$
$\text{iRMSD} = \text{Interface RMSD} \quad (20)$	

Figure 1 Structural parameters used in this work. (A) Labeling the atoms, illustration on a fictitious 2D complex. The binding patch on each partner consists of one layer of atoms (\mathcal{I} , colored solid balls), as identified by a Voronoi interface model [10, 35]. The non interface atoms (\mathcal{I}^c) are split into those which retain solvent accessibility (SASA > 0, dashed balls), and those which do not (SASA = 0, dotted balls) (B) Each interface atom is assigned an integer, its shelling order, equal to the smallest number of atoms traveled to reach an exposed non interface atom, i.e. an atom belonging to \mathcal{I}^c and with SASA > 0 (in grey) [5]. (C,D) The volume of an atom is defined as the volume of the intersection between its ball in the solvent accessible model, and its Voronoi cell [9], a quantity well defined even if the atom retains solvent accessibility. The packing of this atom is the inverse of this volume. Practically, interfaces and binding patches are computed with `Vorshe11`[35], while atomic surface areas and volumes are computed with `Vorlume`[9]. Both programs are available from the Structural Bioinformatics Library (SBL), see <http://sbl.inria.fr>.

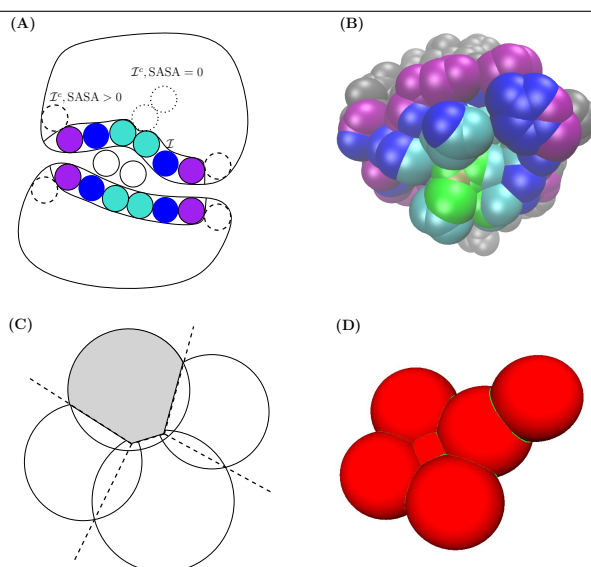


Figure 2 Running binding affinity predictions for a dataset \mathcal{D} i.e. a subset of the structure affinity benchmark: graphical outline of the statistical methodology. (Templates) From the pool of variables, templates are generated. **(Cross-validation)** Each template undergoes a number N_{XV} of repetitions of 5-fold cross-validation, yielding one binding affinity prediction per complex for each repetition. **(Statistics)** Various statistics are computed to assess the performances yielded by the predictive model associated to each template. **(Model selection)** Predictive models are compared, and the best ones selected.

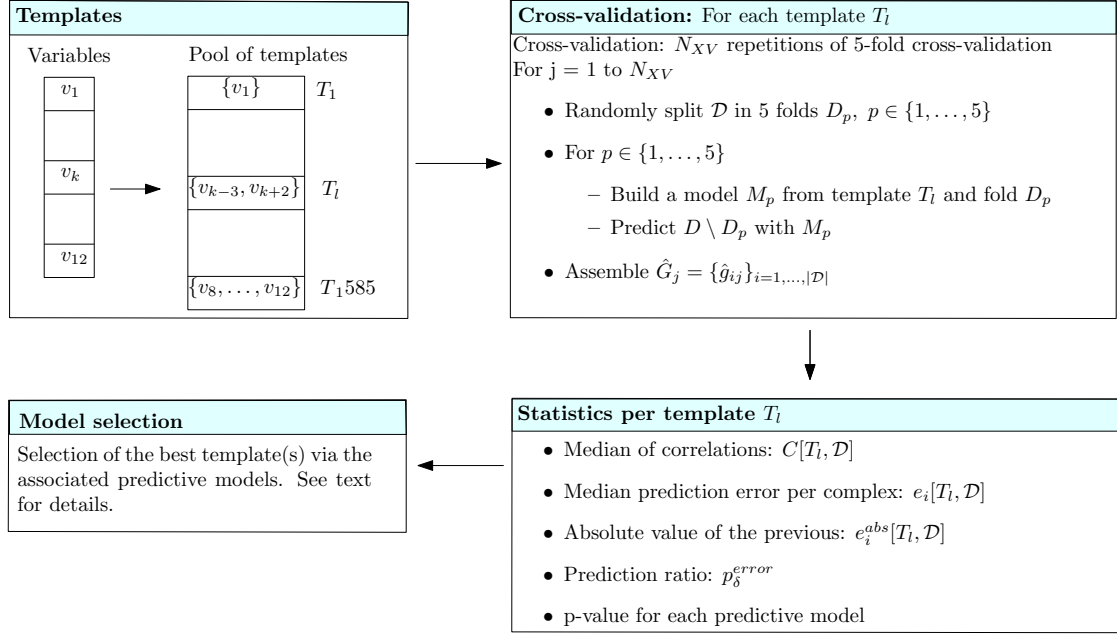


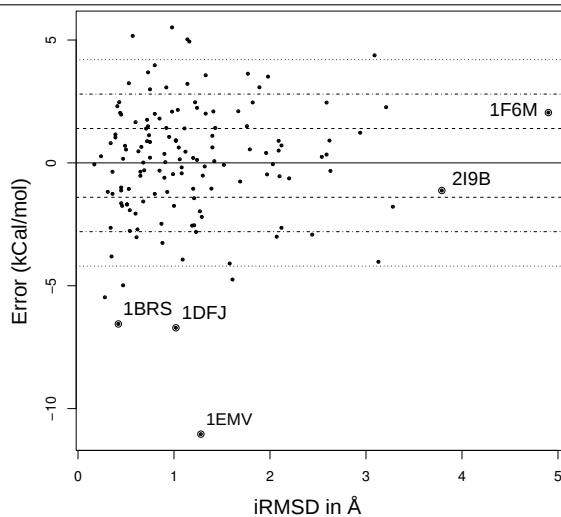
Table 2 Parameters used by the best predictive model for a given dataset. A *dataset* is a subset of the structure affinity benchmark. A *specific* predictive model is the predictive model which performed significantly better than all the others for a given dataset during model selection. The parameters are those from Table 1. Black dots mark variables used by statistically significant predictive models and white dots those used by other predictive models. The last column counts the number of statistically significant predictive models using a given parameter. Asterisks identify atomic level parameters.

	Predictive Model 1 SAB-A	Predictive Model 2 SAB-A-HR	Predictive Model 3 SAB-R _{1.0}	Predictive Models 4 and 9 SAB-R _{1.1}	Predictive Model 5 SAB-R _{1.5}	Predictive Model 6 SAB-I	Predictive Model 7 SAB-F ₁	Predictive Model 8 SAB-F _{1.5}	Counts
iRMSD			•						1
IVW-IPL*	•		•	•	•		•	•	6
SVD_SO1*			•	•				•	3
SVD_SOGT1*		•							1
SVD_NI_E*							•		1
SVD_NI_B*		•				◦			1 (2)
NIS ^{polar}					•				1
NIS ^{charged}	•	•	•	•			•		5
Δ NIS ^{polar}						◦			(1)
Δ NIS ^{charged}									
ATOM_SOLV*		•					•	•	3
POLAR_SASA*									

Table 3 Datasets and their specific predictive models: performances in estimating the dissociation free energy ΔG_d . Each predictive model (rows) was tested on each dataset (columns). A cell in the Table features the values of the affinity prediction ratio $p_{1,4}^{\text{error}}$, $p_{2,8}^{\text{error}}$ and $p_{4,2}^{\text{error}}$ respectively, see Eq. (7). For instance, Predictive Model 1, when evaluated on dataset SAB-A (139 complexes) predicted 47.48%, 78.42% and 92.09% of the complexes with a median absolute error below 1.4, 2.8 and 4.2 kcal/mol, respectively. Equivalently, these are the fractions of cases such that K_d is estimated within one, two and three orders of magnitude. (**Top part**) Previously, these are the fractions of cases with Rep. (replica) were obtained using the values of the parameters provided in the SAB for [30] and those provided by the authors (personal communication) for [33], along with their respective protocols. Lines not marked with Rep. were obtained using the variables of the original models, within our setup. (**Bottom part**) Our predictive models. Bold values indicate when a predictive model was tested on its specific dataset.

	SAB-A	SAB-A-HR	SAB-R _{1,0}	SAB-R _{1,1}	SAB-R _{1,5}	SAB-I	SAB-F ₁	SAB-F _{1,5}
(1) [30, Janin, rep]	29.63, 60.74, 77.78	-	-	37.33, 76.00, 92.00	-	37.04, 62.96, 85.19	-	6.06, 24.24, 39.39
(2) [30, Janin]	39.57, 64.75, 80.21	44.12, 72.06, 92.65	37.18, 73.08, 91.03	39.05, 71.43, 90.48	39.57, 64.75, 80.21	37.14, 71.43, 88.57	32.35, 67.65, 85.29	21.62, 56.76, 86.49
(3) [33, Kastrius, rep]	46.85, 76.92, 90.21	-	41.67, 80.56, 90.28	-	46.62, 81.66, 91.74	-	-	41.18, 61.76, 85.29
(4) [33, Kastrius]	46.76, 75.54, 88.49	51.35, 75.68, 94.59	45.59, 80.88, 91.18	48.72, 80.77, 93.59	47.62, 82.86, 91.43	46.76, 75.54, 88.49	50.00, 72.86, 85.71	47.06, 67.65, 85.29
(5) Predictive Model 1	47.48, 78.42, 92.09	56.76, 86.49, 94.59	54.41, 77.94, 92.65	53.85, 80.77, 91.03	47.62, 79.05, 91.43	44.44, 62.96, 85.19	44.29, 77.14, 82.86	47.06, 70.59, 97.06
(6) Predictive Model 2	47.48, 77.70, 90.65	62.16, 89.19, 97.30	41.18, 76.47, 89.71	44.87, 79.49, 88.46	40.95, 76.19, 90.48	29.63, 70.37, 85.19	47.14, 77.14, 88.57	55.88, 73.53, 91.18
(7) Predictive Model 3	48.92, 78.42, 91.37	54.05, 83.78, 94.59	51.47, 82.35, 92.65	55.13, 79.49, 91.03	45.71, 80.95, 91.43	37.04, 70.37, 88.89	48.57, 74.29, 91.43	52.94, 79.41, 91.18
(8) Predictive Models 4 and 9	48.20, 79.14, 91.37	51.35, 86.49, 94.59	57.35, 79.41, 91.18	55.13, 79.49, 91.03	43.81, 77.14, 91.43	40.74, 66.67, 88.89	48.57, 74.29, 92.86	52.94, 79.41, 91.18
(9) Predictive Model 5	42.45, 76.98, 89.93	56.76, 81.08, 89.19	57.35, 79.41, 89.71	55.13, 80.77, 88.46	45.71, 80.00, 89.52	40.74, 74.07, 88.89	47.14, 75.71, 88.57	41.18, 70.59, 85.29
(10) Predictive Model 6	37.41, 64.03, 87.05	37.84, 64.86, 83.78	36.76, 55.88, 88.24	34.62, 56.41, 87.18	37.14, 66.67, 85.71	44.44, 70.37, 88.89	35.71, 68.57, 87.14	32.35, 67.65, 88.24
(11) Predictive Model 7	48.92, 79.14, 91.37	59.46, 83.78, 91.89	54.41, 77.94, 91.18	52.56, 78.21, 91.03	46.67, 79.05, 91.43	37.04, 66.67, 85.19	50.00, 78.57, 90.00	50.00, 73.53, 94.12
(12) Predictive Model 8	38.85, 74.82, 89.93	32.43, 70.27, 89.19	48.53, 79.41, 88.24	44.87, 78.21, 87.18	39.05, 74.29, 89.52	33.33, 74.07, 88.89	47.14, 72.86, 90.00	50.00, 79.41, 85.29

Figure 3 The hardness of predicting a binding affinity does not correlate with the flexibility of the complex. *x*-axis: flexibility of the interface, expressed in terms of interface iRMSD; *y*-axis: median prediction error $e_i[T_i, \mathcal{D}]$ (Eq. (5)). Dashed, dash-dotted and dotted lines respectively show errors of ± 1.4 , ± 2.8 , ± 4.2 kcal/mol, corresponding to K_d approximated within one, two and three orders of magnitude.



References

- [1] R. Bahadur, P. Chakrabarti, F. Rodier, and J. Janin. A dissection of specific and non-specific protein-protein interfaces. *JMB*, 336(4):943–955, 2004.
- [2] D. Blow. *Outline of crystallography for biologists*. Oxford University Press, 2002.
- [3] J.-D. Boissonnat and M. Yvinec. *Algorithmic geometry*. Cambridge University Press, UK, 1998. Translated by H. Brönnimann.
- [4] L. Bonetta. Protein-protein interactions: Interactome under construction. *Nature*, 468(7325):851–854, 2010.
- [5] B. Bouvier, R. Grunberg, M. Nilgès, and F. Cazals. Shelling the Voronoi interface of protein-protein complexes reveals patterns of residue conservation, dynamics and composition. *Proteins: structure, function, and bioinformatics*, 76(3):677–692, 2009.
- [6] B.R. Brooks, R.E. Bruccoleri, B.D. Olafson, D.J. States, S. Swaminathan, and M. Karplus. CHARMM: A program for macromolecular energy, minimization, and dynamics calculations. *Journal of computational chemistry. Volume 4, Issue 2, Pages 187 - 217*, 1983.
- [7] F. Cazals and T. Dreyfus. SBL, the Structural Bioinformatics Library, 2015. <http://sbl.inria.fr>.
- [8] F. Cazals, T. Dreyfus, D. Mazaauric, A. Roth, and C.H. Robert. Conformational ensembles and sampled energy landscapes: Analysis and comparison. *Journal of Computational Chemistry*, 36(16):1213–1231, 2015.
- [9] F. Cazals, H. Kanhere, and S. Lorient. Computing the volume of union of balls: a certified algorithm. *ACM Transactions on Mathematical Software*, 38(1):1–20, 2011.
- [10] F. Cazals, F. Proust, R. Bahadur, and J. Janin. Revisiting the Voronoi description of protein-protein interfaces. *Protein Science*, 15(9):2082–2092, 2006.
- [11] T.C. Chalikian. Volumetric properties of proteins. *Annual review of biophysics and biomolecular structure*, 32(1):207–235, 2003.
- [12] C.A. Chia-en, W. Chen, and M.K. Gilson. Ligand configurational entropy and protein binding. *PNAS*, 104(5):1534–1539, 2007.
- [13] C. Chipot. Frontiers in free-energy calculations of biological systems. *Wiley Interdisciplinary Reviews: Computational Molecular Science*, 4(1):71–89, 2014.
- [14] John D Chodera and David L Mobley. Entropy-enthalpy compensation: role and ramifications in biomolecular ligand recognition and design. *Biophysics*, 42, 2013.
- [15] C. Chothia and J. Janin. Principles of protein-protein recognition. *Nature*, 256:705–708, 1975.
- [16] W. Cornell, P. Cieplak, C. Bayly, I. Gould, K. Merz, D. Ferguson, D. Spellmeyer, T. Fox, J. Caldwell, and P. Kollman. A second generation force field for the simulation of proteins, nucleic acids, and organic molecules. *Journal of the American Chemical Society*, 117(19):5179–5197, 1995.

- [17] DWJ. Cruickshank. Remarks about protein structure precision. *Acta Crystallographica Section D: Biological Crystallography*, 55(3):583–601, 1999.
- [18] J. Dunitz. Win some, lose some: enthalpy-entropy compensation in weak intermolecular interactions. *Chemistry & biology*, 2(11):709–712, 1995.
- [19] D. Eisenberg and A.D. McLachlan. Solvation energy in protein folding and binding. *Nature*, 319:199–203, 1986.
- [20] David Eisenberg, Morgan Wesson, and Mason Yamashita. Interpretation of protein folding and binding with atomic solvation parameters. *Chem. Scr. A*, 29:217–221, 1989.
- [21] A. Erijman, E. Rosenthal, and J.M. Shifman. How structure defines affinity in protein-protein interaction. *PLOS one*, 9(10), 2014.
- [22] D. Frenkel and B. Smit. *Understanding molecular simulation*. Academic Press, 2002.
- [23] M. Gerstein and F.M. Richards. Protein geometry: volumes, areas, and distances. In M. G. Rossmann and E. Arnold, editors, *The international tables for crystallography (Vol F, Chap. 22)*, pages 531–539. Springer, 2001.
- [24] M.K. Gilson and H-X. Zhou. Calculation of protein-ligand binding affinities. *Annual review of biophysics and biomolecular structure*, 36(1):21, 2007.
- [25] A. Golbraikh and A. Tropsha. Beware of q²! *Journal of Molecular Graphics and Modelling*, 20(4):269–276, 2002.
- [26] M. Guharoy and P. Chakrabarti. Conservation and relative importance of residues across protein-protein interfaces. *PNAS*, 102(43):15447–15452, Oct 2005.
- [27] W.F. Van Gunsteren and H.J.C. Berendsen. Groningen molecular simulation (GROMOS). *Library manual, Biosmos, Groningen, The Netherlands*, pages 1–221, 1987.
- [28] L. Györfi and A. Krzyzak. *A distribution-free theory of nonparametric regression*. Springer, 2002.
- [29] N. Horton and M. Lewis. Calculation of the free energy of association for protein complexes. *Protein Science*, 1(1):169–181, 1992.
- [30] J. Janin. A minimal model of protein-protein binding affinities. *Protein Science*, 23(12):1813–1817, 2014.
- [31] J. Janin, R. P. Bahadur, and P. Chakrabarti. Protein-protein interaction and quaternary structure. *Quarterly reviews of biophysics*, 41(2):133–180, 2008.
- [32] P.L. Kastritis, I.H. Moal, H. Hwang, Z. Weng, P.A. Bates, A. Bonvin, and J. Janin. A structure-based benchmark for protein-protein binding affinity. *Protein Science*, 20:482–491, 2011.
- [33] P.L. Kastritis, J.P.G.L.M. Rodrigues, G.E. Folkers, R. Boelens, and A.M.J.J. Bonvin. Proteins feel more than they see: Fine-tuning of binding affinity by properties of the non-interacting surface. *J.M.B.*, 426:2632–2652, 2014.
- [34] S.M. Lippow, K.D. Wittrup, and B. Tidor. Computational design of antibody-affinity improvement beyond in vivo maturation. *Nature biotechnology*, 25(10):1171–1176, 2007.

- [35] S. Lorient and F. Cazals. Modeling macro-molecular interfaces with Intervor. *Bioinformatics*, 26(7):964–965, 2010.
- [36] M. Lu and J. Ma. The role of shape in determining molecular motions. *Biophysical journal*, 89(4):2395–2401, 2005.
- [37] G. Meng, N. Arkus, M.P. Brenner, and V.N. Manoharan. The free-energy landscape of clusters of attractive hard spheres. *Science*, 327(5965):560–563, 2010.
- [38] I. Moal and J. Fernández-Recio. Comment on *protein-protein binding affinity prediction from amino acid sequence*. *Bioinformatics (Oxford, England)*, 2014.
- [39] I.H. Moal, R. Agius, and P.A. Bates. Protein–protein binding affinity prediction on a diverse set of structures. *Bioinformatics*, 27(21):3002–3009, 2011.
- [40] I. Moreira, P. Fernandes, and M.J. Ramos. Hot spots – a review of the protein–protein interface determinant amino-acid residues. *Proteins: Structure, Function, and Bioinformatics*, 68(4):803–812, 2007.
- [41] B. Phipson and G.K. Smyth. Permutation p-values should never be zero: calculating exact p-values when permutations are randomly drawn. *Statistical Applications in Genetics and Molecular Biology*, 9(1), 2010.
- [42] P. Privalov, A. Dragan, and C. Crane-Robinson. Interpreting protein/dna interactions: distinguishing specific from non-specific and electrostatic from non-electrostatic components. *Nucleic acids research*, page gkq984, 2010.
- [43] D. Rajamani, S. Thiel, S. Vajda, and C.J. Camacho. Anchor residues in protein-protein interactions. *PNAS*, 101(31):11287–11292, 2004.
- [44] G. Subba Rao, R. Vijaykrishnan, and M. Kumar. Structure-based design of a novel class of potent inhibitors of inha, the enoyl acyl carrier protein reductase from mycobacterium tuberculosis: A computer modelling approach. *Chemical biology & drug design*, 72(5):444–449, 2008.
- [45] F. Rodier, R.P. Bahadur, P. Chakrabarti, and J. Janin. Hydration of protein - protein interfaces. *Proteins*, 60(1):36–45, 2005.
- [46] H. Schiessel. Counterion condensation on flexible polyelectrolytes: dependence on ionic strength and chain concentration. *Macromolecules*, 32(17):5673–5680, 1999.
- [47] A. Schmidt, H. Xu, A. Khan, T. O’Donnell, S. Khurana, L. King, J. Manischewitz, H. Golding, P. Suphaphiphat, A. Carfi, E. Settembre, P. Dormitzer, T. Kepler, R. Zhang, A. Moody, B. Haynes, H-X. Liao, D. Shaw, and S. Harrison. Preconfiguration of the antigen-binding site during affinity maturation of a broadly neutralizing influenza virus antibody. *PNAS*, 110(1):264–269, 2013.
- [48] R. Tibshirani. Regression shrinkage and selection via the lasso. *Journal of the Royal Statistical Society. Series B (Methodological)*, pages 267–288, 1996.
- [49] K.M. Visscher, P.L. Kastiritis, and A. Bonvin. Non-interacting surface solvation and dynamics in protein–protein interactions. *Proteins*, 83:445–458., 2015.
- [50] D.J. Wales. *Energy Landscapes*. Cambridge University Press, 2003.

- [51] Z. Yand, L. Guo, L. Hu, and J. Wang. Specificity and affinity quantification of protein - protein interactions. *Bioinformatics*, 29(9):1127–1133, 2013.

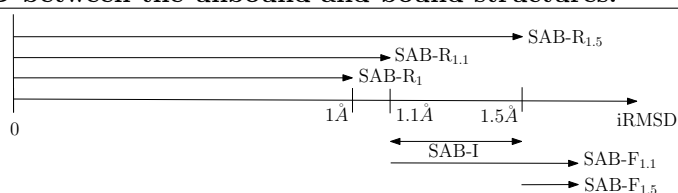
6 Supplemental

6.1 Datasets from the Structure Affinity Benchmark

Curation. To exploit variation of structural parameters between the unbound and bound form, we establish a one-to-one correspondence between the atoms of a partner (from bound to unbound). To cope with cases involving missing residues or atoms, we proceed in two stages. First, we perform an alignment and map residues of the bound and unbound chains. Second, we map atoms of paired residues. We then retain the cases for which at least 80% of atoms are paired. This procedure ruled out two cases, namely 1E6J (78%) and 1ZLI (76%). We also removed three cases (1IQD, 1NSN, 1UUG) for which an upper bound on K_d instead of a proper value is provided for a total of 139 complexes.

Datasets. The various datasets defined in previous works from the SAB are presented on Fig. 4.

Figure 4 The various datasets defined from the structure affinity benchmark (SAB), based on iRMSD between the unbound and bound structures.



The datasets depicted on Fig. 4 are defined as follows:

- SAB-A (139 complexes): all complexes.
- SAB-R_{1.0} (68 complexes): (focus on rigidity, strict threshold) complexes characterized by $\text{iRMSD} < 1\text{Å}$ [39] ([33] used $\text{iRMSD} \leq 1\text{Å}$, 69 complexes).
- SAB-R_{1.1} (78 complexes): (focus on rigidity, intermediate threshold) complexes characterized by $\text{iRMSD} < 1.1\text{Å}$ [30].
- SAB-R_{1.5} (105 complexes): (focus on rigidity, relaxed threshold) complexes characterized by $\text{iRMSD} \leq 1.5\text{Å}$ [33].
- SAB-I (27 complexes): (intermediate complexes) complexes characterized by $1.1 \leq \text{iRMSD} \leq 1.5\text{Å}$ [30].
- SAB-F₁ (70 complexes): (focus on flexibility, relaxed threshold) complexes characterized by $\text{iRMSD} > 1\text{Å}$ [51] ([39] used $\text{iRMSD} \geq 1\text{Å}$, 71 complexes)
- SAB-F_{1.5} (34 complexes): (focus on flexibility, strict threshold) complexes with $\text{iRMSD} > 1.5\text{Å}$ [30][33].

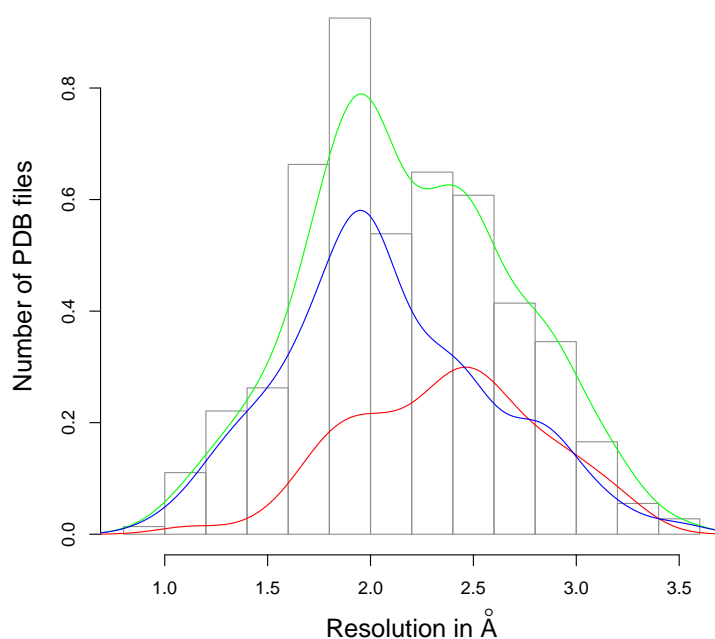
To which we add:

- SAB-A-HR (37 complexes): high resolution complexes from [21]

6.2 Resolution of Crystal Structures in the Affinity Benchmark

The distribution of resolutions of crystal structures found in the SAB is presented on Fig. 5.

Figure 5 Resolution of the structures in the SAB. The histogram and green kernel density estimation curve are for the whole SAB, the red curve is for the complexes and the blue curve is for the unbound partners. For the whole SAB: Minimum = 0.93 Å, median: = 2.13 Å, average = 2.19 Å, max = 3.5 Å. NB: the high resolution dataset SAB-A-HR retains only entries whose resolution is better than 2.5 Å for both the complex and the individual partners [21].



6.3 Methods used in Previous Studies

This section reviews previous work on affinity prediction, in three respects: the type of prediction model used, the variables used, and the statistical methodology.

6.3.1 From reference [39]

Datasets. Seven complexes were discarded from the original affinity benchmark: three because only the upper bound of the affinity was known (1UUG, 1IQD and 1NSN) and four because some features needed by the models were missing (1DE4, 1M10, 1NCA and 1NB5).

Types of models. Affinity values were predicted as the un-weighted average of the output of four different classifiers (random forest, multivariate adaptive regression splines, M5' regression trees and radial basis function interpolation). Each classifier was fed a total of 200 different and possibly correlated features. All classifiers were able to perform feature selection to some extent

and therefore, their actual number of parameter was smaller than 200. In effect, M5' trees use 84 variables, random forest uses 19 variables, MARS uses 10 variables and RBF weights all variable equally and therefore virtually uses all 200 variables. The union of the three first sets contains 94 variables.

Type of variables. The variables used fall into 7 categories:

- Statistical potentials (both atomistic and coarse-grained)
- Solvation and electrostatics (using force fields)
- Entropy terms (translational, rotational, vibrational)
- Contact potentials (H-bonds, π - π interactions, Van der Waals, salt bridges)
- Interface properties (BSA, polarity, geometrical features, surface complementarity)
- Change between bound and unbound states for all of the above
- All of the above computed on an ensemble of structures generated with CONCOORD.

Type of cross validation. On the training set, the correlation between predictions and experimental values was computed using a cross-validation. Complexes from the test set were predicted using the model trained on the validated set. The models were trained on a subset of 57 complexes with further validated affinity values. The predictions were tested on the training dataset using leave-one-out cross-validation. They were further tested on 80 complexes. However, the reported results do not include the correlation between predictions and affinity on the test set alone. Instead, the correlations were reported for the test set + cross-validated train set.

6.3.2 From reference [30]

Datasets. The set of rigid complexes (with iRMSD < 1.1) minus six complexes (1UUG, 2PTC, 1BRS, 2BTF, 1Z0K and 1S1Q) was used to fit the model. In SAB-I, four more complexes were also removed: 1EMV, 1KXP, 1AKJ and 1WQ1.

Type of model. A linear model was fitted on the data using least-square regression.

Type of variables. Two variables were used for that model: iRMSD and the buried surface area. Both are interface properties.

Type of cross-validation. No cross-validation was involved. The correlation between fitted and experimental values was computed on various subset of the SAB and the whole SAB. The results are therefore optimistic on rigid complexes.

Remarks In various datasets, complexes which were badly predicted by the model were removed as outliers. This leads to artificially high correlation coefficients. This is denoted by yellow cells in Table 4.

6.3.3 From reference [51]

This paper first aims at creating a scoring function for docking using statistical parameters. The correlation between the score of a complex and its affinity was also computed.

Dataset. The original full dataset consisted in 3045 complexes extracted from DOCKGROUND, and the training dataset consisted of half of it. Moreover, docking decoys were used as negative examples.

The test set consisted in the SAB without 1UUG, 1IQD, 1NSN, 1DE4, 1M10, 1NCA and 1NB5.

Type of model. The model was based on a scoring function optimized to discriminate between native complexes and decoys. This function used knowledge-based statistical potentials derived from the training set i.e. the probability of a given pair of atoms interacting in a given radius compared to that same probability for non-interacting atoms.

Type of variables. The equivalent of variables for that model were the distance-dependent atom-pair potentials. These were based on observed and expected frequencies of occurrences of atom pairs. From 12 atom types, 78 different pairs occur, and this was computed for 14 different radii, leading to 1092 parameters

Type of cross-validation. No cross-validation was used since the training and test were assumed to be disjoint. It is worth noting however that 24 complexes from the SAB were also part of the 3045 original complexes. Since 1UUG was removed that lets at most 23 complexes shared between the training and test sets.

6.3.4 From reference [33]

Dataset. Only one complex was removed from the SAB, namely 2OZA because “its BSA was extraordinary large and detected as an outlier using the standard Grubbs’ test”

type of model A linear model was fitted on a rigid subset of the SAB using least-square regression. This straining set was defined by complexes with an iRMSD $\leq 1\text{\AA}$.

Type of variables. Three variables were used: the BSA which accounts for interface properties, $NIS^{charged}$ and NIS^{polar} which account for the surface of the complex outside the interface.

Type of cross-validation 4-fold cross-validation was performed to assess the performances of the model on the training set.

Remarks The cross-validation procedure was a less strict strategy than the standard cross validation, where the intersection between the data used to train and test was void. Namely, during the 4-fold cross-validation, the coefficients of the four models trained on their respective folds were averaged to get a single model. The correlation coefficient of the prediction of that model with the actual values was reported. Therefore, through averaging, information about the whole dataset was used for training a model that was tested on the very same dataset, leading to overfitting. This is denoted by an orange cell in Table 4.

Moreover, dataset SAB-I is a superset of the training set. Namely, the model was trained on all complexes with iRMSD $< 1\text{\AA}$ and tested on complexes with iRMSD $< 1.5\text{\AA}$. This is another instance of overfitting. This is denoted by a cyan cell in Table 4.

6.3.5 From reference [21]

Dataset. This paper used the SAB from which ten complexes were filtered out, namely: 1BJ1, 1F34, 1JIW, 1JMO, 1S1Q, 1XD3, 2J0T, 2TGP, 1NVU and 2OZA. It also defined a second dataset consisting of high-resolution entries, i.e. complexes for which both the individual partners and the bound form had a resolution lower than 2.5Å.

Type of model A linear model was fitted on the data using least-square regression.

Type of variables. The variables used consisted in intra and inter-chain hydrogen bond potentials, geometric complementarity (Van der Waals interactions), volume of cavities at the surface (large enough to contain water molecules), iRMSD for interface, C- α and side-chains χ_1 and χ_2 dihedral angles, alanine-scanning defined hotspots, interface amino-acid propensities and electrostatics (Coulomb). In total the combinations of 13 variables were studied. The authors mentioned that adding more than four variables did not significantly improve the results, but the reported correlation coefficient seem to be for models of 7 or more variables after figure 5 of the paper. Which variables were actually selected was not mentioned.

Type of cross-validation. The reported correlation coefficients were computed using leave-one-out cross-validation.

6.4 Statistical Methodology

This section details our algorithms.

6.4.1 Algorithms

Algorithm 1 Computing a permutation p-value for a binding affinity predictive model specified by a template T_l . The p-value is based on a permutation test [41], which uses the prediction performances obtained on random datasets, each such dataset being obtained by permuting the dependent variable (i.e. the affinity) over the dataset.

Require: \mathcal{D} : dataset; T_l : a template; p_{T_l} : a performance criterion for T_l ; $N_{\text{perm.}}$: number of repetitions

for $q \in \{1 \dots N_{\text{perm.}}\}$ **do**

Randomly permute the dependent variable in \mathcal{D} (here the affinity) to obtain $\mathcal{D}_q^{\text{perm}}$

Perform 5-fold cross-validation of linear models using the variables in T_l on $\mathcal{D}_q^{\text{perm}}$

Store the performance criterion in $p_{T_l}^{\text{perm}}$

Report the approximate p-value for T_l to be $\frac{B+1}{N_{\text{perm.}}+1}$, with B the number of elements in $p_{T_l}^{\text{perm}}$ which are more extreme than p_{T_l} .

Algorithm 2 Model selection: identifying specific predictive models for a dataset \mathcal{D} .

The algorithm returns the index of the last predictive model which cannot be distinguished from the best ones given their performance criterion distribution. It is assumed that the predictive models are sorted in non-decreasing order by their median performance criterion. In short, the algorithm executes a binary search, shrinking the interval by its end when there is a significant difference between the predictive models in the interval, and expanding it by its end when there is no difference. All shrink/expand events are applied at the end of the interval to only keep the best predictive models in the final set. Storing the smallest upper bound encountered so far and stopping when it is equal to the upper bound ensures that the algorithm finishes.

Require: $P = \{\mathcal{P}_{T_l}, l \in \{1 \dots 1585\}\}$: the set of distributions of the performance criterion for each template T_l , sorted by non-decreasing median value; cutoff: a cutoff for the p-value of the Kruskal - Wallis test.

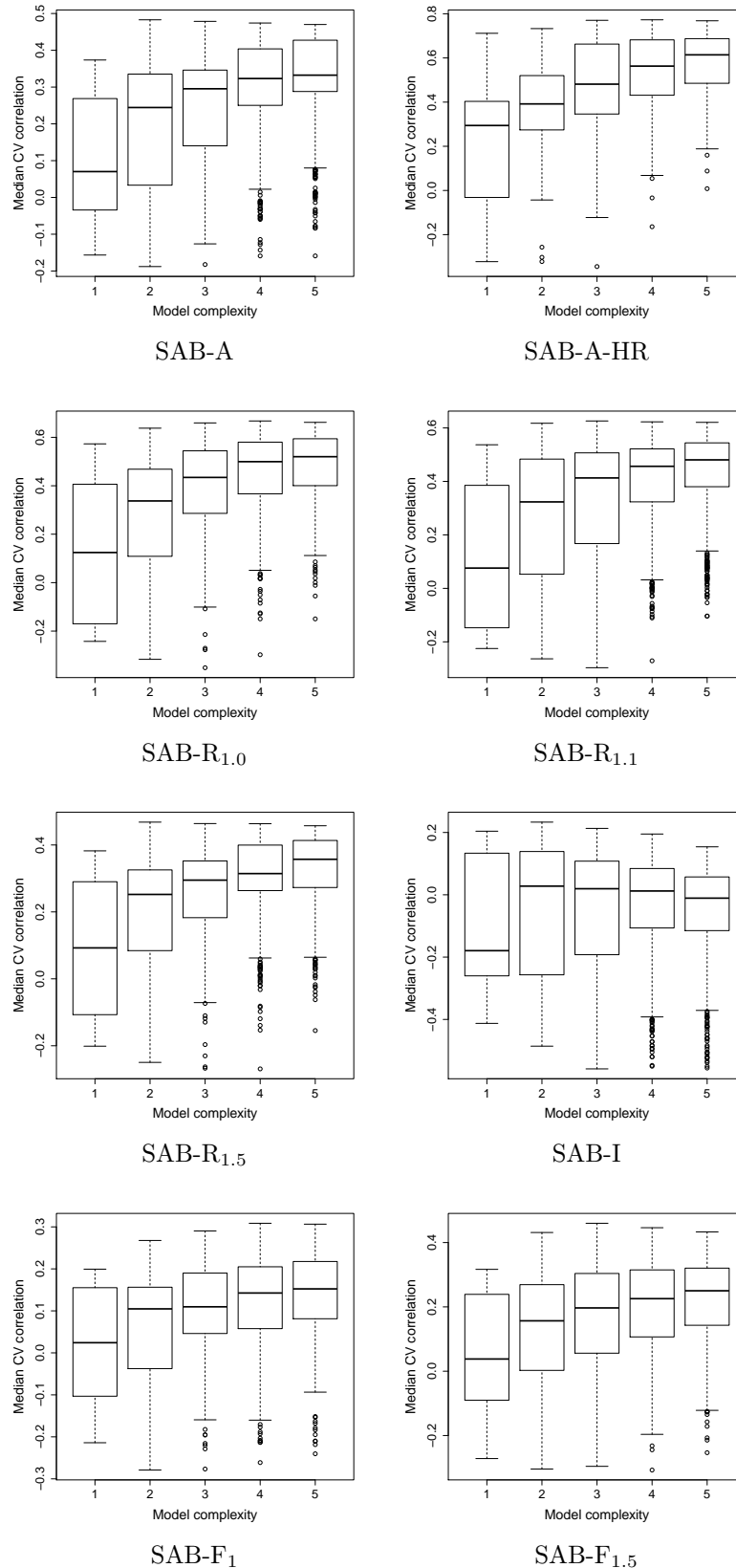
```

start := 0
end := |P|
while TRUE do
   $P_{min} := \{\mathcal{P}_{T_l}, i \in \{start, \dots, end\}\}$ 
  Perform Kruskal - Wallis' test on  $P_{min}$ . Store the p-value in  $p$ .
  if  $p < cutoff$  then
    ## Shrink toward best predictive models
    end :=  $\lceil |P_{min}|/2 \rceil$ 
  else
    ## Expand toward worse predictive models
    tmp := start
    start := end
    end := end +  $\lfloor (end - start)/2 \rfloor$ 
  if end > |P| then
    ## All predictive models are equivalent
    return(|P|)
  if start = end then
    ## the shrinking / expanding process has converged
    if  $p \geq cutoff$  then
      ## The final pivot is part of the similar distributions
      return(end)
    else
      ## The final pivot is part of the outliers
      return(end - 1)
  if end = 1 then
    ## Only one remains (after a sequence of shrinkings only)
    return(end)

```


6.4.2 Predictive models and their Complexity

Figure 6 Predictive model complexity versus median correlation C_V between predicted and experimental values.



6.4.3 Computing Correlation and Prediction Errors for Repeated Cross-validation

For a given predictive model, our validation protocol results in N_{XV} predictions for each complex. This can be seen as a $139 \times N_{XV}$ matrix \hat{G} where each entry \hat{g}_{ij} is the prediction for complex i obtained at repetition j . From the experimental values $\Delta G_d^{exp_i}$, there are therefore two ways to get a single value for the correlation and prediction error per complex.

As a first option, one can agglomerate all N_{XV} predictions into a single value by taking their median. This is \hat{g}_i defined in Eq. 4 and repeated hereunder for convenience:

$$\hat{g}_i = \text{median}_j \hat{g}_{ij}. \quad (21)$$

Then it is straightforward to compute the correlation between $\{\Delta G_d^{exp_i}\}$ and $\{\hat{g}_i\}$:

$$C[T_l, \mathcal{D}] = \text{Corr}(\{\Delta G_d^{exp_i}\}, \{\hat{g}_i\}) \quad (22)$$

and the prediction error for complex i :

$$e_i[T_l, \mathcal{D}] = \Delta G_d^{exp_i} - \hat{g}_i \quad (23)$$

As a second option, one can take the median of the correlations (resp. prediction errors) over the repetitions. Let $Corr_j$ be the correlation coefficient associated with repetition j , i.e. the correlation between $\{\Delta G_d^{exp_i}\}$ and $\{\hat{g}_{ij}\}$ for a given j . This results in equations 3 and 5, repeated here for convenience:

$$C[T_l, \mathcal{D}] = \text{median}_j Corr_j. \quad (24)$$

$$e_i[T_l, \mathcal{D}] = \text{median}_j (\Delta G_d^{exp_i} - \hat{g}_{ij}) \quad (25)$$

We chose the second method because it makes more sense to us to compute median over statistics than over predictions. Moreover, for a given complex i , the ordering of values \hat{g}_{ij} and $\Delta G_d^{exp_i} - \hat{g}_{ij}$ is the same. We therefore have that $\text{median}_j (\Delta G_d^{exp_i} - \hat{g}_{ij}) = \Delta G_d^{exp_i} - \hat{g}_i$. For the correlation, the two methods give very similar values and give the highest value to the same predictive model. (Fig. 9).

6.5 Results: Specific Predictive Models

Upon applying the methods described in 2.4, a single best specific predictive model was obtained for each dataset.

- **Predictive Model: 1. Obtained for dataset(s): SAB-A** 2 variables, p-value ≤ 0.0001 .

$$\Delta G_d = \alpha + \beta \cdot \text{IVW-IPL} + \gamma \cdot \text{NIS}^{charged} \quad (26)$$

- **Predictive Model: 2. Obtained for dataset(s): SAB-A-HR** 4 variables, p-value ≤ 0.0001 .

$$\Delta G_d = \alpha + \beta \cdot \text{SVD_SOGT1} + \gamma \cdot \text{SVD_NI_B} + \epsilon \cdot \text{NIS}^{charged} + \zeta \cdot \text{ATOM_SOLV} \quad (27)$$

- **Predictive Model: 3. Obtained for dataset(s): SAB-R_{1,0}** 4 variables, p-value ≤ 0.0001 .

$$\Delta G_d = \alpha + \beta \cdot \text{iRMSD} + \gamma \cdot \text{IVW-IPL} + \delta \cdot \text{SVD_SO1} + \epsilon \cdot \text{NIS}^{charged} \quad (28)$$

- **Predictive Model: 4. Obtained for dataset(s): SAB-R_{1.1}** 3 variables, p-value ≤ 0.0001 .

$$\Delta G_d = \alpha + \beta \cdot \text{IVW-IPL} + \gamma \cdot \text{SVD_SO1} + \delta \cdot \text{NIS}^{\text{charged}} \quad (29)$$

- **Predictive Model: 5. Obtained for dataset(s): SAB-R_{1.5}** 2 variables, p-value ≤ 0.0001 .

$$\Delta G_d = \alpha + \beta \cdot \text{IVW-IPL} + \gamma \cdot \text{NIS}^{\text{polar}} \quad (30)$$

- **Predictive Model: 6. Obtained for dataset(s): SAB-I** 2 variables, p-value ≤ 0.090 .

$$\Delta G_d = \alpha + \beta \cdot \text{SVD_NI_B} + \gamma \cdot \Delta \text{NIS}^{\text{polar}} \quad (31)$$

- **Predictive Model: 7. Obtained for dataset(s): SAB-F₁** 4 variables, p-value ≤ 0.0091 .

$$\Delta G_d = \alpha + \beta \cdot \text{IVW-IPL} + \gamma \cdot \text{SVD_NI_E} + \delta \cdot \text{NIS}^{\text{charged}} + \epsilon \cdot \text{ATOM_SOLV} \quad (32)$$

- **Predictive Model: 8. Obtained for dataset(s): SAB-F_{1.5}** 3 variables, p-value ≤ 0.0054 .

$$\Delta G_d = \alpha + \beta \cdot \text{IVW-IPL} + \gamma \cdot \text{SVD_SO1} + \delta \cdot \text{ATOM_SOLV} \quad (33)$$

- **Predictive Model: 9. Obtained for dataset(s): All datasets** 3 variables, p-value ≤ 0.0001 for SAB-A, SAB-A_{hr}, SAB-R_{1.0}, SAB-R_{1.1}, SAB-R_{1.5}; ≤ 0.6949 for SAB-I; ≤ 0.0158 for SAB-F₁; $\leq ,0.0089$ for SAB-F_{1.5}.

$$\Delta G_d = \alpha + \beta \cdot \text{IVW-IPL} + \gamma \cdot \text{SVD_SO1} + \delta \cdot \text{NIS}^{\text{charged}} \quad (34)$$

6.6 Results: Correlation and comparison with previous work

See the detailed Table 4.

Table 4 Binding affinities: correlations between predictions and measurements for all datasets and all specific predictive models. (Whole table) Red values show the best results for a given category in the corresponding section, and cross-validated and classical correlation coefficients are treated separately in the second part of the table. Bold values in the second part of the table show the categories on which the variables selection was performed for a given predictive model. (First section) Previous work: values published and our replica (rep). Green cells correspond to the correlation coefficient of the predictive model over the train set (i.e. $\sqrt{R^2}$ from the linear regression). Purple cells correspond to either cross-validation results, prediction on a test set distinct from the trains set, or both. For the other cell colors, see details in supplemental section 6.3. Yellow cells: discrepancies between original values and our replicas – we did not remove any complex. Orange cells: the cross-validation procedure made some test data information leak into the training set. Cyan cells: overlapping training and test sets. (Second section) Eight predictive models developed in this work. The value reported in a cell corresponds to the correlation between predictions and experimental values. For the $N_{XV} = 10000$ 5-fold cross-validation, the median of the predictions was used (see Statistical Methods section 2.4). Purple lines show the cross-validated correlation coefficient, while green lines show the classical correlation coefficient (square root of the coefficient of determination).

Predictive Model	#param	SAB-A	SAB-A-HR	SAB-R _{1,0}	SAB-R _{1,1}	SAB-R _{1,3}	SAB-I	SAB-F ₁	SAB-F _{1.5}
[39]	94 (200) (see section 6.3.1)	0.55	-	0.7	-	-	-	0.36	-
[30] rep	2	0.20	-	-	0.55 (0.62)	-	0.07 (0.38)	-	0.13
[51]	~1000 (see section 6.3.3)	0.39	-	0.63	-	-	-	0.24	-
[33] rep	3	0.48	-	0.58	-	-	-	-	0.34
[21]	7	0.57	0.71	-	-	0.54	-	-	-
Predictive Model 1: selected for datasets SAB-A									
N_{XV} 5-fold CV	2	0.48	0.72	0.64	0.62	0.46	-0.39	0.27	0.39
LOO CV	2	0.48	0.72	0.63	0.61	0.46	-0.57	0.24	0.35
No CV	2	0.52	0.76	0.67	0.64	0.51	0.20	0.37	0.59
Predictive Model 2: selected for datasets SAB-A-HR									
N_{XV} 5-fold CV	4	0.44	0.77	0.52	0.51	0.40	-0.08	0.24	0.31
LOO CV	4	0.44	0.77	0.51	0.51	0.39	-0.16	0.22	0.27
No CV	4	0.50	0.83	0.62	0.60	0.49	0.40	0.40	0.59
Predictive Model 3: selected for datasets SAB-R _{1,0}									
N_{XV} 5-fold CV	4	0.47	0.71	0.67	0.62	0.46	-0.21	0.24	0.42
LOO CV	4	0.46	0.71	0.66	0.62	0.45	-0.31	0.23	0.39
No CV	4	0.52	0.76	0.72	0.67	0.53	0.40	0.41	0.65
Predictive Model 4 and 9: selected for datasets SAB-R _{1,1}									
N_{XV} 5-fold CV	3	0.47	0.71	0.64	0.63	0.46	-0.21	0.28	0.44
LOO CV	3	0.47	0.71	0.63	0.62	0.45	-0.30	0.26	0.41
No CV	3	0.52	0.76	0.68	0.67	0.51	0.35	0.41	0.65
Predictive Model 5: selected for datasets SAB-R _{1,5}									
N_{XV} 5-fold CV	2	0.44	0.64	0.63	0.60	0.47	-0.27	0.25	0.31
LOO CV	2	0.43	0.63	0.62	0.59	0.46	-0.54	0.22	0.28
No CV	2	0.47	0.68	0.66	0.62	0.5	0.12	0.32	0.43
Predictive Model 6: selected for datasets SAB-I									
N_{XV} 5-fold CV	2	0.04	0.39	0.00	0.01	0.14	0.23	-0.11	-0.15
LOO CV	2	-0.04	0.07	0.03	0.02	0.07	0.17	-0.10	-0.18
No CV	2	0.15	0.50	0.18	0.18	0.23	0.43	0.12	0.15
Predictive Model 7: selected for datasets SAB-F ₁									
N_{XV} 5-fold CV	4	0.46	0.69	0.59	0.57	0.43	-0.19	0.31	0.33
LOO CV	4	0.46	0.69	0.59	0.56	0.43	-0.28	0.29	0.28
No CV	4	0.52	0.77	0.67	0.65	0.51	0.34	0.44	0.60
Predictive Model 8: selected for datasets SAB-F _{1.5}									
N_{XV} 5-fold CV	3	0.35	0.46	0.59	0.53	0.36	-0.04	0.20	0.46
LOO CV	3	0.34	0.43	0.58	0.52	0.35	-0.12	0.18	0.45
No CV	3	0.40	0.55	0.64	0.59	0.42	0.29	0.33	0.59

6.7 Results: Correlations between individual variables and/or measured affinity

Table 5 Pearson correlation coefficients between the individual variables and the affinity.

	-0.09	-0.39	-0.39	-0.24	-0.19	-0.1	-0.04	0.01	irmsd
	0.36	0.48	0.59	0.56	0.41	0.11	0.23	0.34	ivwipl
	0.13	0.19	0.01	-0.02	0.04	0.28	0.24	0.36	s_diff_vol_so1
	-0.3	-0.41	-0.49	-0.45	-0.33	-0.12	-0.19	-0.28	s_diff_vol_sogt1
	0.08	0.38	0.06	0.06	0.13	0.35	0.09	-0.07	s_diff_vol_not_int_bur
	0	-0.1	-0.18	-0.16	-0.04	0.25	0.15	0.15	s_diff_vol_not_int_surf
	0.29	0.55	0.37	0.37	0.3	0.05	0.21	0.23	nis_polar
	-0.4	-0.74	-0.51	-0.52	-0.38	0.18	-0.29	-0.49	nis_charged
	-0.13	-0.32	-0.18	-0.17	-0.21	-0.36	-0.09	0.14	nis_polar_diff
	-0.03	0.01	0.02	-0.03	0.02	0.18	-0.08	-0.18	nis_charged_diff
	0.14	0.35	0.23	0.16	0.1	-0.09	0.02	0.33	solvation_eisen
	-0.05	-0.1	0.03	-0.01	-0.02	-0.01	-0.1	-0.1	polar_surf_area
All									
High Res									
IRMSD < 1									
IRMSD < 1.1									
IRMSD <= 1.5									
1.1 <= IRMSD <= 1.5									
IRMSD > 1									
IRMSD > 1.5									

Table 6 Pearson correlation coefficients between the individual variables.

	irmsd	ivwipl	s_diff_vol_so1	s_diff_vol_sogt1	s_diff_vol_not_int_bur	s_diff_vol_not_int_surf	nis_polar	nis_charged	nis_polar_diff	nis_charged_diff	solvation_eisen	polar_surf_area
irmsd	-											
ivwipl	0.18	-										
s_diff_vol_so1	-0.25	0.05	-									
s_diff_vol_sogt1	-0.18	-0.83	0.06	-								
s_diff_vol_not_int_bur	-0.33	-0.06	0.43	0.14	-							
s_diff_vol_not_int_surf	0.09	-0.01	0.1	0.06	0.06	-						
nis_polar	-0.2	-0.04	0.19	0.11	0.08	-0.15	-					
nis_charged	0.2	-0.09	-0.2	0.03	-0.07	0.12	-0.71	-				
nis_polar_diff	0.09	-0.18	-0.08	0.17	-0.1	0.01	0.12	0.01	-			
nis_charged_diff	0.02	0.02	0.05	-0.04	-0.02	-0.16	-0.06	0.23	-0.36	-		
solvation_eisen	-0.07	0.03	-0.19	-0.06	-0.27	0.16	0.34	-0.48	0.04	-0.02	-	
polar_surf_area	0.22	0.14	-0.33	-0.21	-0.59	0.34	-0.09	0.08	0.1	-0.02	0.34	-

6.8 Results: Validation on an External Dataset

Table 7 Validation of the models on an external test set. The external test set from [33, supplemental] was split using the same criteria as those used to define datasets from the structure affinity benchmark, yielding *external datasets*. Each linear model was trained using a specific template on the whole corresponding dataset and used to predict the corresponding external datasets. The first part of the table displays the external dataset size, Pearson coefficients and p-value for each predictive on its external dataset along with $p_{1.4}^{\text{error}}$, $p_{2.8}^{\text{error}}$ and $p_{4.2}^{\text{error}}$. The second part show the values from table the diagonal of tables 3 and 4 for comparison.

	Predictive Model 1 SAB-A	Predictive Model 2 SAB-A-HR	Predictive Model 3 SAB-R _{1.0}	Predictive Model 4 SAB-R _{1.1}	Predictive Model 5 SAB-R _{1.5}	Predictive Model 6 SAB-I	Predictive Model 7 SAB-F ₁	Predictive Model 8 SAB-F _{1.5}
dataset size	51	24	13	16	23	7	38	28
p-value	0.0004	0.0295	0.0022	0.0392	0.0170	0.6034	0.0043	0.2753
correlation	0.47	0.44	0.77	0.52	0.49	0.24	0.45	0.21
$p_{1.4}^{\text{error}}$, $p_{2.8}^{\text{error}}$, $p_{4.2}^{\text{error}}$	11.76, 33.33, 47.06	20.83, 25.00, 41.67	30.77, 30.77, 46.15	31.25, 43.75, 43.75	26.09, 34.78, 43.48	0.00, 14.29, 14.29	5.26, 26.32, 52.63	17.86, 46.43, 60.71
median corr.	0.48	0.77	0.67	0.63	0.47	0.23	0.31	0.46
$p_{1.4}^{\text{error}}$, $p_{2.8}^{\text{error}}$, $p_{4.2}^{\text{error}}$	47.48, 78.42, 92.09	62.16, 89.19, 97.30	51.47, 82.35, 92.65	55.13, 79.49, 91.03	45.71, 80.00, 89.52	44.44, 70.37, 88.89	50.00, 78.57, 90.00	50.00, 79.41, 85.29

Table 8 Validation of the best overall model i.e. model 9 on an external test set. See Table 7 for the statistics presented.

Dataset	SAB-A	SAB-A-HR	SAB-R _{1.0}	SAB-R _{1.1}	SAB-R _{1.5}	SAB-I	SAB-F ₁	SAB-F _{1.5}
dataset size	51	24	13	16	23	7	38	28
p-value	0.0003	0.0727	0.0471	0.0392	0.0565	0.3673	0.0190	0.0155
correlation	0.48	0.37	0.56	0.52	0.40	0.40	0.38	0.45
$p_{1.4}^{\text{error}}$, $p_{2.8}^{\text{error}}$, $p_{4.2}^{\text{error}}$	11.76, 33.33, 49.02	20.83, 37.50, 45.83	30.77, 46.15, 46.15	31.25, 43.75, 43.75	21.74, 34.78, 39.13	14.29, 14.29, 28.57	13.16, 39.47, 50.00	17.86, 39.29, 60.71
median corr.	0.47	0.71	0.64	0.63	0.46	-0.24	0.27	0.42
$p_{1.4}^{\text{error}}$, $p_{2.8}^{\text{error}}$, $p_{4.2}^{\text{error}}$	48.2, 79.14, 91.37	51.35, 86.49, 94.59	57.35, 79.41, 91.18	55.13, 79.49, 91.03	43.81, 77.14, 91.43	40.74, 66.67, 88.89	51.35, 86.49, 94.59	52.94, 79.41, 91.18

6.9 Results: On the Quality of Individual Predictions

Table 9 lists the individual predictions, obtained from Eq. (4).

Table 9 Experimental affinities on a per complex basis: experimental measurements (ΔG_d) versus predictions (\hat{g}_i , Eq. 4). Predictions were generated with predictive Model 1 on dataset SAB-A. The median was taken over the NXV repetitions. Blue values indicate under-predicted complexes (63) and red indicate the over-predicted ones (76). A start denotes complexes with error in the top decile.

PDB ID	Measured	Predicted	PDB ID	Measured	Predicted	PDB ID	Measured	Predicted
1A2K	9.31	10.72	1I4D	7.46	9.55	1XU1	11.18	10.66
1ACB	13.05	12.63	1IB1	9.76	10.65	1YVB	11.17	9.48
1AHW	11.55	11.25	1IBR	12.07	12.32	1Z0K	6.98	10.22
1AK4	6.43	10.00	1IJK	10.42	8.85	1ZHI	9.08	9.09
1AKJ	5.32	10.34 *	1J2J	8.13	8.6	1ZM4	8.03	9.26
1ATN	12.07	10.29	1JIW	15.55	12.55	2A9K	10.25	9.93
1AVX	12.50	12.66	1JMO	9.47	11.74	2ABZ	11.67	11.06
1AVZ	6.55	10.24	1JPS	13.64	11.95	2AJF	10.63	10.27
1AY7	13.23	10.46	1JTG	12.82	13.52	2AQ3	6.71	9.17
1B6C	8.94	9.35	1JWH	11.14	9.17	2B42	12.11	13.86
1BJ1	11.55	12.09	1K5D	12.77	10.22	2B4J	10.86	10.4
1BRS	17.32	10.76 *	1KAC	10.68	11.74	2BTF	7.69	10.68
1BUH	9.70	9.91	1KKL	10.02	9.39	2C0L	9.82	10.73
1BVK	10.53	10.65	1KLU	7.28	9.75	2FJU	7.20	9.35
1BVN	15.06	12.58	1KTZ	8.92	9.95	2GOX	12.08	10.01
1CBW	10.75	11.88	1KXP	12.34	12.79	2HLE	10.09	11.19
1DE4	9.78	10.12	1KXQ	11.54	12.43	2HQS	10.15	13.37
1DFJ	18.05	11.34 *	1LFD	7.79	8.34	2HRK	10.98	10.93
1DQJ	11.67	12.52	1M10	11.24	10.7	2I25	12.28	10.84
1E4K	7.87	10.33	1MAH	14.51	11.49	2I9B	12.93	11.81
1E6E	8.28	10.28	1MLC	9.61	11.27	2J0T	13.34	10.53
1E96	7.42	8.82	1MQ8	7.53	9.02	2JEL	11.59	11.53
1EAW	14.06	12.13	1NB5	13.86	9.77 *	2MTA	7.42	9.73
1EER	15.59	12.67	1NCA	11.02	11.29	2NYZ	12.69	13.19
1EFN	10.12	10.48	1NVU	7.43	10.94	2O3B	15.68	11.65 *
1EMV	18.58	7.54 *	1NVU	7.80	12.18 *	2O0B	5.66	7.47
1EWY	7.43	9.42	1NW9	11.19	10.72	2OOR	10.65	10.72
1EZU	13.77	11.23	1OC0	12.28	10.53	2OUL	11.96	10.9
1F34	14.19	13	1OPH	11.32	11.52	2OZA	11.73	14.81
1F6M	7.60	9.64	1P2C	13.63	11.88	2PCB	6.82	8.79
1FC2	10.43	9.68	1PPE	15.56	12.92	2PCC	7.91	9.07
1FFW	8.09	9.51	1PVH	9.52	10.32	2PTC	18.04	12.57 *
1FLE	12.28	13.21	1PXV	12.97	12.63	2SIC	13.84	13.47
1FQJ	9.79	9.82	1QA9	7.16	8.65	2SNI	15.96	12.15
1FSK	13.12	11.48	1R0R	14.17	13.05	2TGP	7.54	12.7 *
1GCQ	6.51	9.59	1R6Q	8.84	10.94	2UUY	11.26	13.3
1GL1	13.23	12.18	1RLB	8.18	8.83	2VDB	13.40	8.42 *
1GLA	6.76	8.84	1RV6	13.86	9.93	2VIR	12.28	11.02
1GPW	11.32	10.8	1S1Q	4.29	9.8 *	2VIS	7.36	11.34 *
1GRN	9.03	11.5	1T6B	13.10	10.39	2WPT	10.67	5.92 *
1GXD	11.30	10.25	1US7	8.09	8.24	3BP8	11.44	10.44
1H1V	10.20	10.83	1VFB	11.46	12.36	3BZD	9.57	9.39
1H9D	9.18	9.03	1WDW	12.72	10.52	3CPH	8.84	9.55
1HCF	13.08	9.82	1WEJ	12.48	11.3	3SGB	14.51	13.25
1HE8	7.37	8.78	1WQ1	6.62	11.56 *	4CPA	11.32	11.23
1HIA	10.76	11.39	1XD3	8.90	11.14			
1I2M	15.83	13.18	1XQS	7.08	10.71			

Figure 7 Distribution of atomic volumes i.e. volumes of Voronoi restrictions for interface atoms. Red curves denote complexes whose interface lies in the top decile in terms of size (i.e, more than 354 interface atoms).

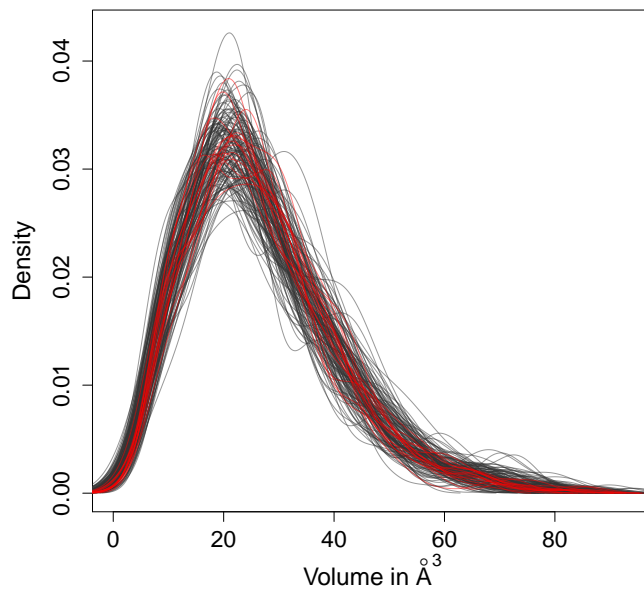


Figure 8 The quality of individual predictions, assessed by $e_i[T_i]$, does not correlate with the interface size.

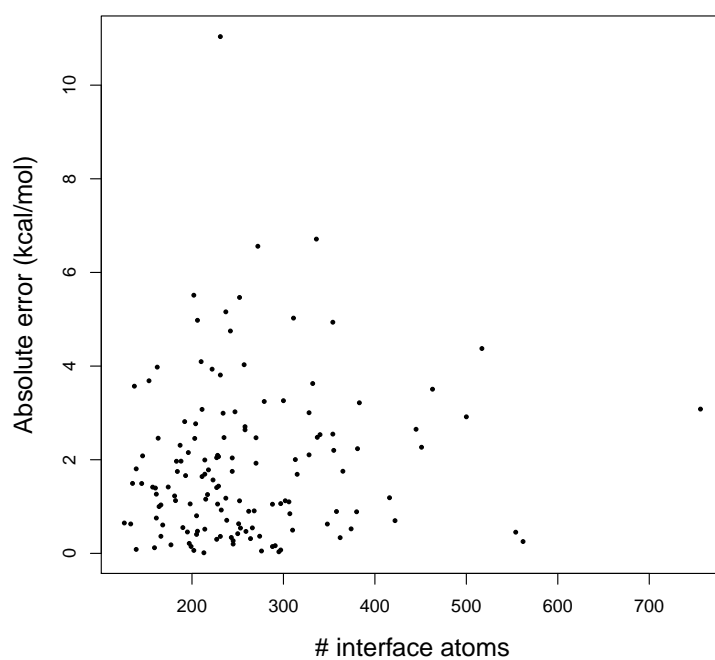
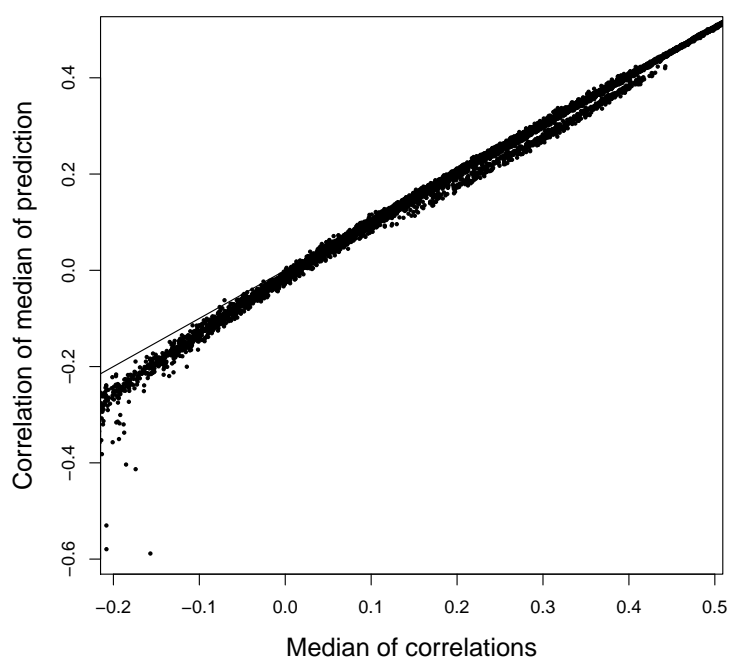


Figure 9 Comparison between two ways of computing the correlation for a given predictive model over multiple repetitions. See details in section 6.4.3. **Median of correlations:** for each of the N_{XV} repeats, compute the correlation between the predictions and experimental affinities. Take the median of these predictions for each complex. **Correlation of median of predictions:** compute a single prediction per complex as the median of all N_{XV} predictions. Compute the correlation between those predictions and the experimental affinities. The values of all predictive models tested on all datasets have been aggregated on this figure. The correlation between both methods is 0.997 with a median absolute difference of 0.005. Moreover, both measures are maximal for the same predictive model on all datasets, i.e. maximizing on either measure will result in the same predictive model selected.





**RESEARCH CENTRE
SOPHIA ANTIPOLIS – MÉDITERRANÉE**

2004 route des Lucioles - BP 93
06902 Sophia Antipolis Cedex

Publisher
Inria
Domaine de Voluceau - Rocquencourt
BP 105 - 78153 Le Chesnay Cedex
inria.fr

ISSN 0249-6399